

# Importance of ice elasticity in simulating tide-induced grounding line variations along prograde bed slopes

Natalya ~~Ross~~<sup>Maslennikova</sup><sup>1</sup>, Pietro Milillo<sup>1,2,3</sup>, Kalyana Nakshatralla<sup>1</sup>, Roberto Ballarini<sup>1</sup>, Aaron Stubblefield<sup>4,5</sup>, Luigi Dini<sup>5,4</sup>

<sup>1</sup>Department of Civil & Environmental Engineering, University of Houston, TX, USA

<sup>2</sup>~~Department of Earth and Atmospheric Sciences, University of Houston, Houston, TX, USA~~

<sup>2,3</sup>German Aerospace Center (DLR), Microwaves and Radar Institute, Munich, Germany

<sup>4,5</sup>~~Earth System Science Interdisciplinary Center, University of Maryland, College Park, MD, USA~~ ~~Thayer School of Engineering, Dartmouth College, Hanover, NH, USA~~

<sup>5,4</sup>Italian Space Agency (ASI), Matera, Italy

Correspondence to: Natalya ~~Maslennikova~~<sup>Ross</sup> ([nmaslenn@cougarnet.uh.edu](mailto:nmaslenn@cougarnet.uh.edu))

**Abstract.** The grounding line, delineating the boundary where a grounded glacier ~~goes-becomes~~ afloat in ocean water, shifts in response to tidal cycles. Here, we analyze COSMO-SkyMed Differential Interferometric Synthetic Aperture Radar (~~DInSAR~~) data acquired in 2020 and 2021 over Totten, Moscow University, and Rennick glaciers in East Antarctica, detecting tide-induced grounding line position variations from 0.5 to 12.5 km along prograde slopes ranging from ~0 to 5%. Considering a glacier as a non-Newtonian fluid, we provide two-dimensional formulations of ~~the~~-viscous and viscoelastic short-term behavior of a glacier ~~while~~ in partial frictional contact with the bedrock, and partially floating on sea-water. Since the models' equations are not amenable to analytical treatment, numerical solutions are obtained using FEniCS, an open-source Python package ~~for solving partial differential equations using the finite element method~~. We establish the dependence of the grounding zone width on glacier thickness, bed slope, and glacier flow speed. The predictions of the viscoelastic model match ~~~97~~<sup>73</sup>% of all the DInSAR grounding zone measurements and are ~~~74~~<sup>44</sup>% more accurate than those of the ~~purely~~ viscous model. ~~The results of This study underscores the critical role played by ice elasticity in continuum mechanics-based glacier models; and demonstrates how these models can be being-validated with-the-using DInSAR measurements, can-be-used-in-other-studies-on glaciers.~~

## 1. Introduction

The grounding line, which ~~delineates defines~~ the ~~transition boundary~~ between the ~~bedrock-based~~ ice sheet ~~(the portion of a glacier laying on the bedrock)~~ and the ~~floating~~ ice shelf ~~(the portion floating on the ocean water)~~, is ~~crucial for of particular significance for comprehensive~~ Antarctic ~~research investigations~~ (Friedl et al., 2020; Haseloff and Sergienko, 2018). ~~This boundary is a fundamental~~ ~~The grounding line is a crucial~~ indicator of glacier stability, as its position reflects the ~~salient~~ glacier dynamics and influences the overall glacier force and mass balances (Davison et al., 2023; Holland, 2008). Grounding lines not only provide valuable information about glacier stability by enabling the evaluation of ice thickness, but also allow ~~for~~ the monitoring of sea level changes due to climate ~~warming-change~~ (Goldstein et al., 1993; Schoof, 2007). ~~Mmechanisms~~ governing variations in grounding line position ~~is-are~~ complex and involves both long-term and short-term processes (Sergienko and Haseloff, 2023; Sergienko, 2022). ~~Here we~~

~~focus on~~ Short-term grounding line migrations are induced by tidal forces and occurring within a tidal cycle (Albrecht et al., 2006; Coleman et al., 2002), while long-term migrations depend primarily on changes in ice dynamics and climate (Freer et al., 2023; Lowry et al., 2024). ~~Differential Interferometric Synthetic Aperture Radar (DInSAR) and altimeter techniques applied across various Antarctic glaciers have shown that the magnitude of tide-induced grounding line migrations can extend to several kilometers; several orders of magnitude wider than the grounding zone width expected from hydrostatic equilibrium (Begeman et al., 2020; Brancato et al., 2020; Brunt et al., 2010; Dawson. Long-term glacier Mmodels primarily aim to estimate of~~ grounding line evolution over time scales significantly exceeding tidal scales, ~~thus neglecting~~ short-term variations (Cornford et al., 2020; Gagliardini et al., 2016; Seroussi et al., 2014). Conversely, short-term glacier models focus on tidal time scales and tend to disregard the long-term evolution of glaciers due to its negligible impact over these shorter periods (Rosier et al., 2014; Rosier and Gudmundsson, 2020). Here, we focus on short-term, tide-induced grounding line migrations, which can extend up to several kilometers (Brancato et al., 2020; Brunt et al., 2010; Dawson and Bamber, 2017; Milillo et al., 2022; Minchew et al., 2017).

~~Several s~~ Short-term glacier dynamics models, employing various ~~has been studied using different~~ physical approaches, have been developed to interpret tide-induced migrations. For example, a hydrological model proposed by Warburton et al. (2020) defines the grounding zone width as the penetration depth into a subglacial cavity of water interacting with an elastic ice beam that responds to ~~the~~ ocean tides. Sayag and Worster (2011, 2013) describe a grounding line migration ~~is considered as the~~ result of ~~the~~ tidal force-induced deformation of an (elastic) Euler-Bernoulli beam, which moves vertically in response to the periodic tidal forces. ~~However, they treat the Young's modulus of ice as a tidal phase-dependent model parameter to support the sustainability of the beam model in fitting the satellite observations.~~ Tsai and Gudmundsson (2015) consider a grounding zone as an opening and closing of a crack between an elastic ice beam and the bedrock, using equations governing the propagation of a water-filled crack under pressure. This model (Tsai and Gudmundsson, 2015), which cannot predict grounding line migrations at low tides, was modified and applied to the Amery Ice Shelf in Antarctica by Chen et al. (2023), who showed that ~~the a~~ crack model can reproduce a kilometer grounding line retreat over a tidal cycle. Nevertheless, the crack-based method is one-dimensional, as it ~~takes into account~~ considers only the glacier motion along the ice-bedrock surface ~~and does not without~~ describing motion-induced changes ~~inside within~~ the ice.

Other previously proposed short-term models treat glacier ice as a viscous or viscoelastic fluid, ~~and seek aiming~~ to determine grounding line migration by resolving contact forces at the base (Stubblefield et al., 2021). Rosier et al. (2014) and Rosier and Gudmundsson (2020) developed designed nonlinear viscoelastic models on tidal time scales, where ~~the~~ normal stress and velocity determine the grounding line position. However, ~~but~~ being considered after discretization, these factors they are not incorporated included into the variational formulation ~~used~~. This technical detail was addressed by Stubblefield et al. (2021), who used the full Navier-Stokes equations for purely viscous flow and included contact conditions in the variational formulation. However, Stubblefield et al. (2021) did not compare the outputs of the viscous model with grounding zone width measurements. Here, we extend the viscous model, proposed by Stubblefield et al. (2021), by incorporating an elastic component within the framework of the upper-convected Maxwell model (Gudmundsson, 2011; Snoeijer et al., 2020). The model formulation utilizes variational

inequalities derived from the governing equations using boundary conditions on ice velocity and normal stress. The variational inequalities are transformed into variational equalities via a penalty method. Grounding line migrations are calculated by solving these variational equations at each time step using the Finite Element Method (FEM) in the open-source FEniCS package (Alnæs et al., 2015; Logg et al., 2012). Glacier thickness, bedrock slope, and ice flow serve as model inputs, and are set based on BedMachine Antarctica (Morlighem et al., 2017) and MEaSUREs InSAR-based ice velocity map of Antarctica (Rignot et al., 2017). We compare ~~model results of automatically generated grounding zones with the~~ grounding zone width measurements from Cosmo-SkyMed Differential Interferometric Synthetic Aperture Radar (DInSAR) data acquired between 2020 and 2021 over East Antarctica. Specifically, we focus on Totten (TOT), Moscow University (MU), and Rennick (REN) glaciers, which are characterized by kilometric tide-induced grounding line migrations. Comparing modelled and DInSAR-based grounding zones, values, manually assessed from the DInSAR interferograms, we evaluate both models' performance and assess the significance of the elastic component relative to the formulation that accounts for only viscosity. Additionally, we determine the impact the ice-bed system's main parameters, namely, bedrock slope, glacier thickness, and ice velocity, on the magnitude of tidally induced grounding line migrations.

## **2. Data and methods**

### **1.1.2.1. Study area**

~~This study focuses on three glaciers, MU, TOT, and REN, whose relative locations in Antarctica are shown in We assess the models' performance using grounding zone, glacier thickness, bedrock slope, and ice flow velocity values that characterize Rennick (REN), Moscow University (MU), and Totten (TOT) glaciers (Figure 1).~~ MU and TOT are neighboring glaciers, located on the Sabrina Coast in East Antarctica (Bensi et al., 2022; Fernandez et al., 2018; Orsi and Webb, 2022). Together, the combined effect of these two glaciers may result in ~~to~~ up to a 5-meter sea level rise, making them major contributors to sea level changes in East Antarctica (Mohajerani et al., 2018). Being characterized by the highest outflow and thinning rate in East Antarctica, TOT also has the third-largest ice flux among all Antarctic glaciers, following Pine Island and Thwaites glaciers (Pritchard et al., 2009; Rignot and Thomas, 2002; Roberts et al., 2018). In contrast, MU exhibits relatively slow thinning rates (Mohajerani et al., 2018) and nearly half the basal melt rate of TOT:  $4.7 \pm 0.8$  m/yr vs  $10.5 \pm 0.7$  m/yr between 2003 and 2008, respectively (Rignot et al., 2013). Both glaciers are grounded below the sea level, making them potentially unstable and susceptible to collapse (Van Achter et al., 2022; Aitken et al., 2016).

REN, situated in Northern Victoria Land in East Antarctica, spans over 400 km along the flow and narrows from 80 km to 25 km across the flow (Allen et al., 1985; Mayewski et al., 1979; Meneghel et al., 1999; Sturm and Carryer, 1970). Containing the sea-level equivalent of 11 cm in ~~the~~ form of ice, REN is also grounded below the sea level and is experiencing rapid thinning due to intensive basal melt (Pritchard et al., 2012; Rignot et al., 2019). REN's ice discharge has shown up to 20% amplification between 1999 and 2018 (Miles et al., 2022). ~~Although REN behaves similarly~~ ~~Despite exhibiting similar behavior~~ to TOT and MU, ~~REN-it~~ retreats slower than most Antarctic glaciers, rendering it relatively stable (Miles et al., 2022; Pritchard et al., 2012).

### **2.2. Glacier parameters used as model inputs**

Since the model requires glacier thickness, bed slopes, and ice speed as input parameters, we estimated these values for the three glaciers of interest. To achieve this, we determined 69 profile lines: 33 lines over MU, 17 over TOT, and 19 over REN (Figure 1).

### **2.2.1. SAR-based ice flow velocities**

The profiles were oriented in the direction of ice flow, derived from the SAR-based ice velocity map of Antarctica (Rignot et al., 2017), provided by NASA's MEaSUREs program. This dataset includes the  $v_x$  and  $v_y$  components of the ice velocities  $\mathbf{v}$  in m/year, projected to EPSG3031 at 450 m resolution. The direction of the ice flow was calculated as  $\arctan(v_y/v_x)$  in degrees and shown with black arrows in Figure 1. Flow lines were selected along the flow direction and were spaced 500 to 600 m apart. Each profile is approximately 20 km long, as this length was adopted as the glacier domain length for the modeling process. The flow lines, and consequently the selected profiles, are not always parallel to the grounding lines, indicating the influence of crossflow heterogeneity in our analysis. To estimate the flow speed, we calculated the magnitude of the ice flow vectors (or the velocity map) as  $\sqrt{v_x^2 + v_y^2}$ . We extracted the values from the velocity map along the profile lines, and computed the average ice flow for each profile. The summary of the calculated ice flow velocities along the selected 69 profiles is provided in Table S1.



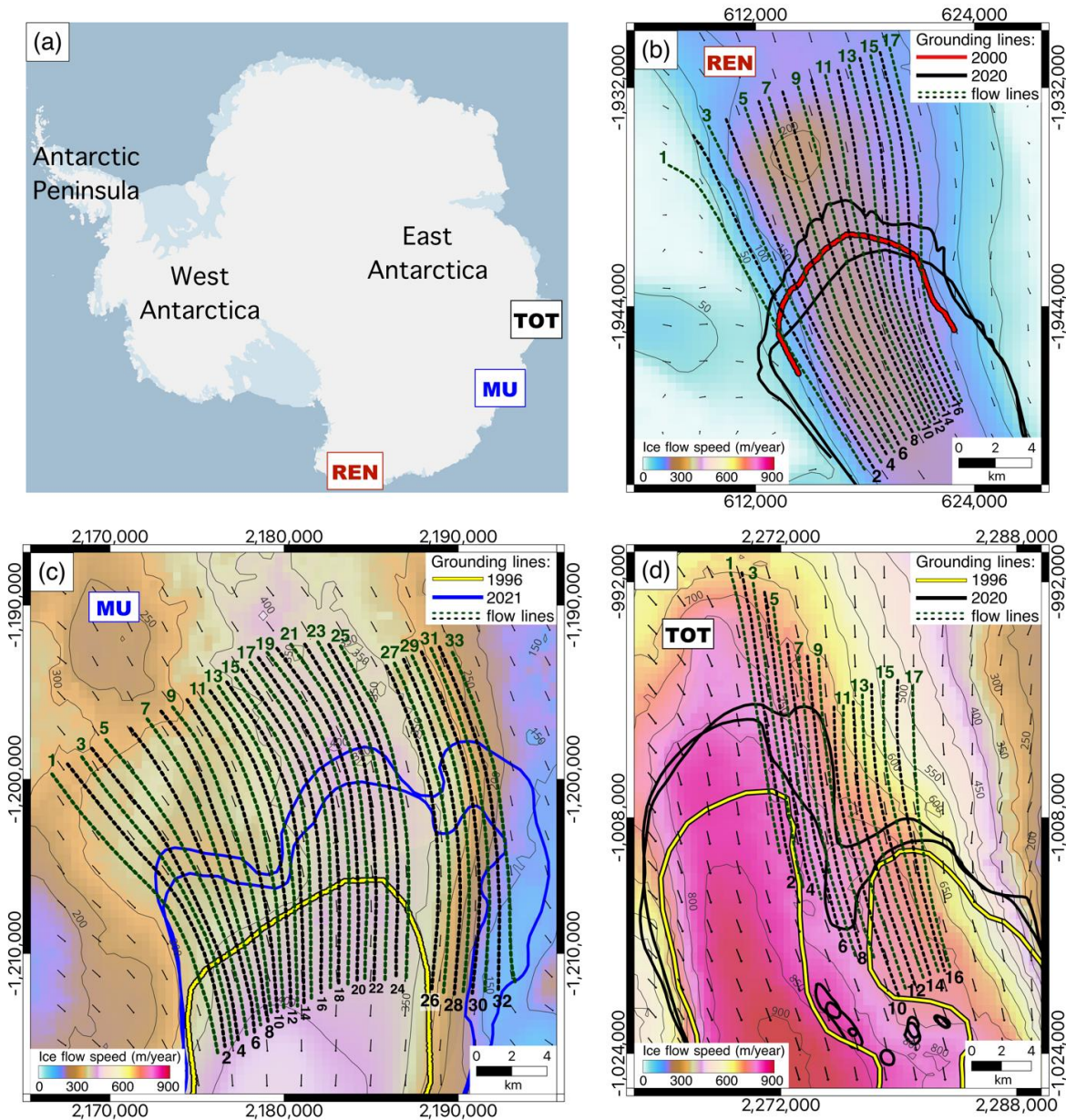


**Figure 1.** Study area: (a) location of Totten (TOT), Moscow University (MU), and Rennick (REN) glaciers in Antarctica; and ice velocity map over b) REN, c) MU, d) TOT. The selected 69 profiles are shown as dashed green and black lines over the black ice flow vectors, derived from the MEaSUREs InSAR-based ice velocity map of Antarctica (Rignot et al., 2017). For visualization purposes, the flow vectors shown here were calculated over a velocity flow map resampled at 2 km, while the directions of the profiles were determined over the original 450 m resolution flow map to maximize the accuracy of the flow direction definition. Subplots (b), (c), (d) show the bed elevation relief from BedMachine2 with 50 m contour levels (purple) over REN, MU, and TOT, respectively. Subplots (e), (f), (g) show the ice thickness map with 100 m contour levels (purple) from BedMachine2 over REN, MU, and TOT, respectively. Subplots (h), (i), (j) show the ice flow velocity map with 20 m/year contour levels (purple) from MEaSUREs2 over REN, MU, and TOT, respectively. Subplots (k), (l), (m) show the DInSAR interferogram at low

135 tide with a corresponding grounding line as a solid line and a grounding line at high tide as a dashed line over REN,  
136 MU, and TOT, respectively. Subplots (n), (o), (p) show the DInSAR interferogram at high tide with a corresponding  
137 grounding line as a solid line and a grounding line at low tide as a dashed line over REN, MU, and TOT, respectively.  
138 The grounding lines over REN and TOT were mapped in 2020 (black line), while the grounding lines over MU (blue  
139 line) correspond to 2021. The grounding lines for 1996 (yellow line) and 2000 (red line) on figures (b) — (j) were taken  
140 from MEaSURES2 DInSAR-based Antarctic grounding line dataset (Rignot et al., 2016). Numbered dark green dotted  
141 lines represent the flow lines, along which the measurements (Table S1) were performed. All datasets maps are  
142 represented in Antarctic projection (EPSG:3031).

### 143 **2.2.2. Ice thickness and bed slope**

144 Glacier thickness values were determined using the 500 m-resolution ice thickness map from BedMachine Antarctica  
145 (version 2) (Morlighem et al., 2017), as shown in Figure 2. Thickness values were extracted along the profiles, and  
146 the average thickness was calculated for each profile. Bed slopes for each profile were determined using the 500 m-  
147 resolution BedMachine Antarctica topographic map (Figure 2) by linearly approximating extracted bed elevation  
148 values and calculating the slope of the fitted line. The summary of the calculated glacier thicknesses and bed slopes  
149 along the selected 69 profiles is provided in Table S1.

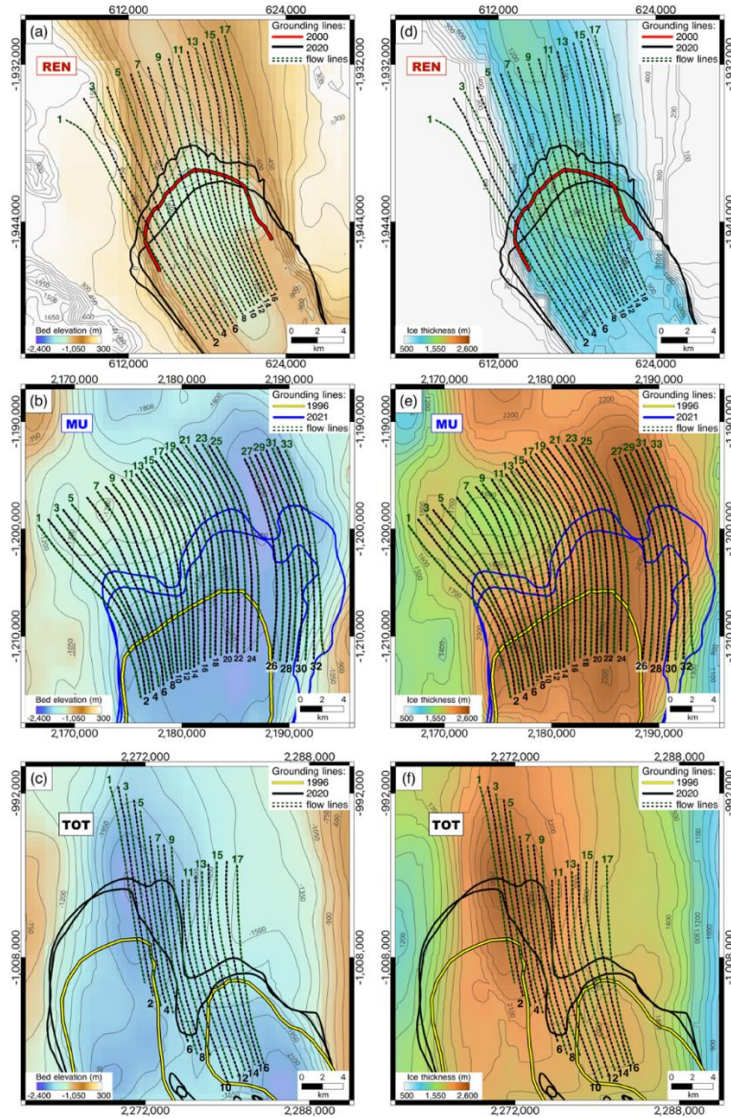


**Figure 2.** Bed elevation relief from BedMachine2 (Morlighem et al., 2017) over a) REN, b) MU, c) TOT; and ice thickness maps from BedMachine2 (Morlighem et al., 2017) over d) REN, e) MU, and f) TOT. The selected 69 profiles are shown as dashed green and black lines. The grounding lines over REN and TOT were mapped in 2020 (black line), while the grounding lines over MU (blue line) correspond to 2021. The grounding lines for 1996 (yellow line) and 2000 (red line) were taken from MEaSUREs2 DInSAR-based Antarctic grounding line dataset (Rignot et al., 2016). All maps are represented in Antarctic projection (EPSG:3031).

### 2.2.3. DInSAR-based grounding widths for model validation

As the model estimates grounding zone values, grounding zone measurements are required to assess the model performance. We obtained the grounding zone width values for TOT, MU, and REN by utilizing a series of 1-day repeat pass Synthetic Aperture Radar (SAR) data from the COSMO-SkyMed (CSK) mission, operated by the Italian Space Agency (ASI). The first generation of the mission which comprises a constellation of four satellites



~~constellation~~ equipped with synthetic aperture radars operating at X-band with a wavelength of 3.1 cm (Milillo et al., 2014). Each of the four ~~first-generation~~ satellites has a 16-day repeat cycle, while ~~our analysis focuses on the images collected by the second and third satellites~~, capture InSARing data over the same area with a 1-day interval. Interferograms were generated using GAMMA software (Werner et al., 2000) from CSK STRIPMAP data, following a validated processing chain (Brancato et al., 2020; Milillo et al., 2017). Satellite acquisitions were designed as a set of five consecutive overlaying  $40 \times 40$  km swath frames with an azimuth and range resolution of 3 meters. To eliminate topographic effects, the Copernicus digital elevation model (DEM) is employed. To co-register the data and achieve maximum phase coherence, we used satellite orbits for coarse co-registration and used a pixel offsets approach for fine co-registration. A multi-looking factor of 10 in both range and azimuth was used to achieve an interferogram resolution of 30 m x 30 m. Two one-day interferometric pairs were combined into one double differential interferogram (DInSAR) to cancel out horizontal deformation due to glacier flow. Each interferometric pair combined in a double difference DInSAR interferogram ~~was is~~ acquired within 1.5 months over the same satellite track ~~in order to~~ minimize horizontal velocity changes and highlight vertical glacier motion, enabling grounding line mapping (Milillo et al., 2022). Double difference DInSAR interferograms from different orbits acquired at different times ensured sensitivity to several frequencies of the tidal spectrum (Milillo et al 2017, Minchew et al 2017).

An interferometric fringe corresponds to half a wavelength of surface displacement, equivalent to 1.5 cm of satellite line of sight displacement per fringe for X-band or about 1.7 cm when projecting deformation onto the vertical considering the satellite incidence angle. The grounding line can be manually delineated as the most inner fringe in the grounded ice side. Therefore, the DInSAR technique provides information about vertical tide-induced glacier movements and enables grounding line mapping with an average empirically determined manual mapping accuracy of ~~the order of~~ 100 - 200 m (Rignot et al., 2014; Ross et al., 2024). To connect the models with the observations, we needed to link every SAR image to its unique sea level and atmospheric pressure level, which also introduced vertical displacement due to the inverse barometer effect (IBE) (Padman et al., 2002). The IBE correction was performed by examining anomalies in mean sea level pressure, reconstructed using the fifth generation of the European Centre for Medium-Range Weather Forecasts (ECMWF) atmospheric reanalysis dataset of the global climate (ERA-5; Table S6) (Hersbach et al., 2020). The tidal heights during the acquisition of the SAR images were determined using the Circum-Antarctic Tidal Simulation (CATS2008) model (Padman et al., 2002) and listed in Table S6. Despite that one double difference DInSAR interferogram is a combination of four SAR images, characterized by four different sea levels, one DInSAR interferogram provided only one grounding line measurement. A high tide lifts the glacier, allowing seawater to penetrate under the glacier, while a low tide causes the glacier to readvance. Following Milillo et al. (2022), we assumed that the grounding line position observed in a DInSAR interferogram corresponds to the largest combination of tidal level and IBE among the four SAR acquisitions. To estimate the grounding zone width for one glacier, we used a pair of double difference DInSAR interferograms. A maximum acquisition gap of 1.5 months between the interferograms in a pair ensures that any variations in the grounding line position occurs due to the tidal interaction rather than glacier retreat (Milillo et al., 2022). The difference between the largest IBE-corrected tidal heights (Column H in Table S6) in each pair of DInSAR interferograms is 0.95 m for MU, 1.03 m for TOT, and 1.08 m for REN (Column  $\Delta H$  in Table S6). For each pair of interferograms, the interferogram with the higher H value



represents the inland position of the grounding line and corresponds to the ocean tide, referred to as ‘high tide’ in the model. Conversely, the interferogram with the lower H value represents the outward position of the grounding line, corresponding to ‘low tide’ in the model. To ensure a valid comparison between the DInSAR-derived grounding zones and the modeled grounding zones, the IBE-corrected tidal levels listed in column H of Table S6 are used to evaluate the grounding zone width in the model. We measure the modeled grounding zone widths by calculating the difference between the grounding line position at maximum H and at minimum H.

Combining two manually mapped grounding lines for each interferogram in a pair, we established a grounding zone for the corresponding glacier and measure the grounding zone widths along the selected profiles ~~see flow directions~~. Therefore, one pair of DInSAR interferograms for MU, allowed us to obtain 33 grounding zone width values, as 33 profiles were originally selected over this glacier. Analogously, we obtained 19 grounding zone widths for REN, and 17 for TOT. Taking the higher limit of the grounding line mapping error of 200 m (Rignot et al., 2014; Ross et al., 2024), we determined the largest level of uncertainty of 400 m for each grounding zone measurement due to error propagation (see measurements error bars in Figure 6 (c)). The summary of the grounding zone width measurements is provided in Table S1, the grounding zone width measurement process for MU, TOT, and REN is visualized in Figure 3, which shows all three pairs of DInSAR interferograms, corresponding to low and high tide, and the 69 profiles along which the grounding zone width measurements were performed.

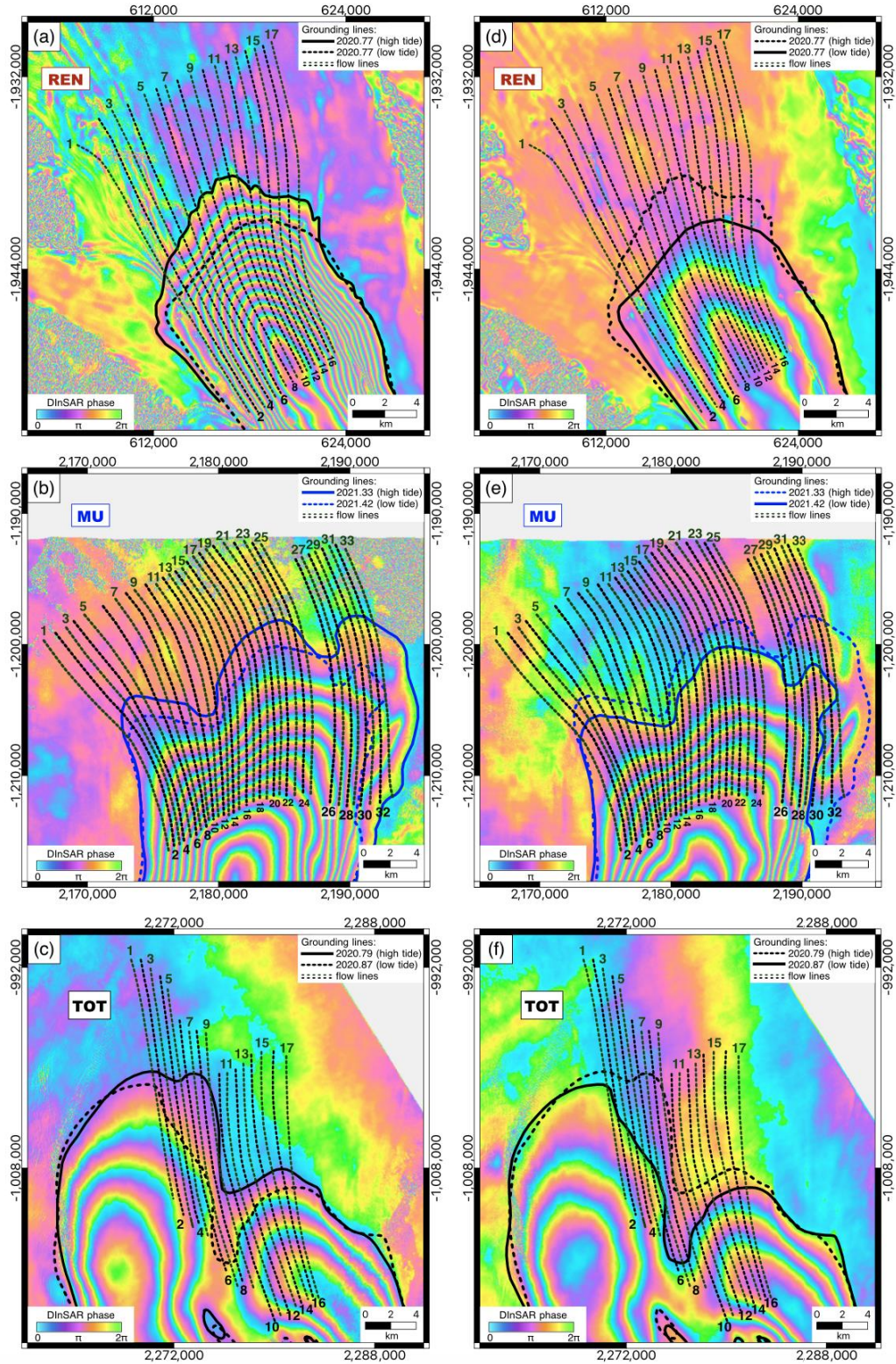


**Figure 3.** Pairs of DInSAR interferograms over a) REN, b) MU, c) TOT at high tide, and over d) REN, e) MU, f) TOT at low tide with corresponding manually mapped grounding lines. All interferograms are represented in Antarctic projection (EPSG:3031).

**Figure 1.** Study area: (a) location of Totten (TOT), Moscow University (MU), and Rennick (REN) glaciers in Antarctica. Subplots (b), (c), (d) show the bed elevation relief from BedMachine2 with 50 m contour levels (purple) over REN, MU, and TOT, respectively. Subplots (e), (f), (g) show the ice thickness map with 100 m contour levels (purple) from BedMachine2 over REN, MU, and TOT, respectively. Subplots (h), (i), (j) show the ice flow velocity map with 20 m/year contour levels (purple) from MEaSUREs2 over REN, MU, and TOT, respectively. Subplots (k), (l), (m) show the DInSAR interferogram at low tide with a corresponding grounding line as a solid line and a grounding line at high tide as a dashed line over REN, MU, and TOT, respectively. Subplots (n), (o), (p) show the DInSAR interferogram at high tide with a corresponding grounding line as a solid line and a grounding line at low tide as a dashed line over REN, MU, and TOT, respectively. The grounding lines over REN and TOT were mapped in 2020 (black line), while the grounding lines over MU (blue line) correspond to 2021. The grounding lines for 1996 (yellow line) and 2000 (red line) on figures (b) — (j) were taken from MEaSUREs2 DInSAR based Antarctic grounding line dataset. Numbered dark green dotted lines represent the flow lines, along which the measurements (Table S1) were performed. All datasets are represented in Antarctic projection (EPSG:3031).

## 2.3. Viscous and viscoelastic models

The short-term grounding line migration model, rooted in the Navier-Stokes equations under the assumption of viscoelastic ice flow, builds upon is based on the purely viscous formulation of the same problem (Stubblefield et al., 2021). Here, we provide the comprehensive description of the viscoelastic model along with a comparison between the viscous and viscoelastic models, summarize the similarities and differences between the models, while the comprehensive description of the viscoelastic model including the derivation of the model's penalized problem (A35), and the details about the models comparison are provided in Appendix A: Glacier modelling.

### 3.1. Principal notation

The notation used in the paper is listed in Table 1 and is further explained during the model formulation. In addition to summarizing the quantities and their corresponding mathematical symbols, Table 1 also provides the units and identifies the field type to which each quantity belongs, such as scalar, vector, or tensor field.

Notation, used in the paper, is listed in Table A1.

**Table 1.** Models' principal notation

Symbol	Quantity	Field type	Units
<b>Geometry-related quantities</b>			
$(X, Y)$	<u>laboratory coordinate system</u>	<u>2D coordinate system</u>	$(m, m)$
$x = (x, y)$	<u>spatial point <math>x</math> with coordinates <math>x</math> and <math>y</math></u>	<u>Point in 2D space</u>	$(m, m)$
$\Omega$	<u>2D glacier domain</u>	<u>2D spatial domain</u>	$(m, m)$
$\partial\Omega$	<u>boundary of the glacier domain</u>	<u>Geometric boundary</u>	$m$
$\Gamma_D$	<u>inflow boundary</u>	<u>Geometric boundary</u>	$m$
$\Gamma_N$	<u>outflow boundary</u>	<u>Geometric boundary</u>	$m$
$\Gamma_a$	<u>ice–air surface</u>	<u>Geometric boundary</u>	$m$
$\Gamma_b$	<u>ice–bedrock surface</u>	<u>Geometric boundary</u>	$m$

$\Gamma_w$	<u>ice–water surface</u>	<u>Geometric boundary</u>	$m$
$\Gamma_s$	<u>lower glacier boundary</u>	<u>Geometric boundary</u>	$m$
$h(x, t)$	<u>surface elevation of the ice shelf</u>	<u>Scalar</u>	$m$
$s(x, t)$	<u>lower boundary of the ice shelf</u>	<u>Scalar</u>	$m$
$\alpha$	<u>bedrock slope</u>	<u>Scalar</u>	$\%$
$b(x)$	<u>bedrock slope function</u>	<u>Scalar</u>	$m$
$A$	<u>bedrock inclination parameter</u>	<u>Scalar</u>	$m$
$L$	<u>glacier length</u>	<u>Scalar</u>	$m$
$H(t)$	<u>glacier thickness</u>	<u>Scalar</u>	$m$
$l(t)$	<u>sea level</u>	<u>Scalar</u>	$m$
$\hat{n}(x)$	<u>unit outward normal vector at point <math>x</math> of a domain boundary</u>	<u>Vector</u>	$-$
<b><u>Materials properties</u></b>			
$\rho_i$	<u>ice density</u>	<u>Scalar</u>	$kg \cdot m^{-3}$
$\rho_w$	<u>water density</u>	<u>Scalar</u>	$kg \cdot m^{-3}$
$\phi$	<u>friction</u>	<u>Scalar</u>	$Pa \cdot s \cdot m^{-1}$
$C$	<u>friction coefficient</u>	<u>Scalar</u>	$Pa \cdot \left(\frac{s}{m}\right)^{\frac{1}{n}}$
$\eta$	<u>ice viscosity</u>	<u>Scalar</u>	$Pa \cdot s$
$G$	<u>shear modulus</u>	<u>Scalar</u>	$Pa$
$\lambda$	<u>relaxation time</u>	<u>Scalar</u>	$s$
$n$	<u>stress exponent (from the Glen's flow law)</u>	<u>Scalar</u>	$-$
$A$	<u>ice softness</u>	<u>Scalar</u>	$Pa^{-n} \cdot s^{-1}$
<b><u>Physical quantities</u></b>			
$t$	<u>time</u>	<u>Scalar</u>	$s$
$p$	<u>ice pressure</u>	<u>Scalar</u>	$Pa$
$p_w$	<u>water pressure at the ice–water interface</u>	<u>Scalar</u>	$Pa$
$p_w^0$	<u>hydrostatic water pressure</u>	<u>Scalar</u>	$Pa$
$v_0$	<u>inflow speed on <math>\Gamma_D</math></u>	<u>Scalar</u>	$m \cdot s^{-1}$
$v$	<u>ice flow velocity</u>	<u>Vector</u>	$m \cdot s^{-1}$
$g$	<u>acceleration due to gravity</u>	<u>Vector</u>	$m \cdot s^{-2}$
$D$	<u>strain rate tensor</u>	<u>Tensor</u>	$s^{-1}$
$T$	<u>Cauchy stress tensor</u>	<u>Tensor</u>	$Pa$
$\tau$	<u>deviatoric stress tensor</u>	<u>Tensor</u>	$Pa$
<b><u>Mathematical operators</u></b>			
$\mathbb{I}$	<u>identity tensor</u>	<u>Tensor</u>	$-$
$\mathbb{P}$	<u>orthogonal projection onto the boundary</u>	<u>Tensor</u>	$-$
$\nabla$	<u>spatial gradient operator</u>	<u>Operator</u>	$m^{-1}$
$\nabla \cdot$	<u>spatial divergence operator</u>	<u>Operator</u>	$m^{-1}$
$\cdot$	<u>inner (dot) product</u>	<u>Operator</u>	$-$
$\otimes$	<u>tensor product</u>	<u>Operator</u>	$-$
$\overset{\nabla}{\tau}$	<u>upper-convected time derivative of some tensor field (in this case, of the tensor <math>\tau</math>)</u>	<u>Operator</u>	$Pa \cdot s^{-1}$
<b><u>Model numerical parameters</u></b>			



$\delta \ll 1$	<u>Glen's flow law numerical parameter, used to prevent model numerical instabilities</u>	<u>Scalar</u>	$s^{-2}$
$\varepsilon \ll 1$	<u>Numerical parameter in the friction expression, used to prevent numerical instabilities</u>	<u>Scalar</u>	$m^2 \cdot s^{-2}$

### 3.2. Glacier domain

For both models, we designate the glacier domain as  $\Omega$ , as shown in Figure 4, with a piece-wise smooth boundary  $\partial\Omega$ . We place the glacier in ~~the a~~ two-dimensional coordinate system  $(X, Y)$ , where  $X$  denotes the horizontal axis, and  $Y$  is used for identifying the vertical axis. In the principal notation used in this paper, a spatial point is denoted by  $\mathbf{x} = (x, y) \in \bar{\Omega}$ , where an overline denotes the set closure. For glacier length  $L$ , the ice domain  $\Omega$  can be mathematically expressed as

$$\Omega = \left\{ (x, y): |x| < \frac{L}{2}, s(x, t) < y < h(x, t) \right\} \quad (1)$$

The glacier boundary is represented as a union of five complementary parts:

$$\partial\Omega = \Gamma_D \cup \Gamma_N \cup \Gamma_w \cup \Gamma_b \cup \Gamma_a, \quad (2)$$

where  $\Gamma_D$  is an inflow boundary,  $\Gamma_N$  is an outflow boundary,  $\Gamma_w$  is an ice–water surface,  $\Gamma_b$  is an ice–bedrock surface, and  $\Gamma_a$  is an ice–air surface. Defining  $f(x)$  as a bedrock slope function,  $h(x, t)$  as a time-dependent function of the glacier surface elevation, and  $s(x, t)$  as a function, defining the position of lower boundary of the ice shelf with time, the ice–water and ice–bed boundaries are expressed as

$$\Gamma_w = \{(x, y) \in \partial\Omega: y = s(x, t) > f(x)\}, \quad (3)$$

$$\Gamma_b = \{(x, y) \in \partial\Omega: y = s(x, t) = f(x)\}. \quad (4)$$

The entire lower boundary  $\Gamma_s$  therefore, is identified as a union of the ice–water and ice–bed boundaries:

$$\Gamma_s = \Gamma_w \cup \Gamma_b = \{(x, y) \in \partial\Omega: y = s(x, t) \geq f(x)\} \quad (5)$$

The grounding line position is identified as ~~the a~~ point, where the ice–water boundary intersects the ice–bed boundary.

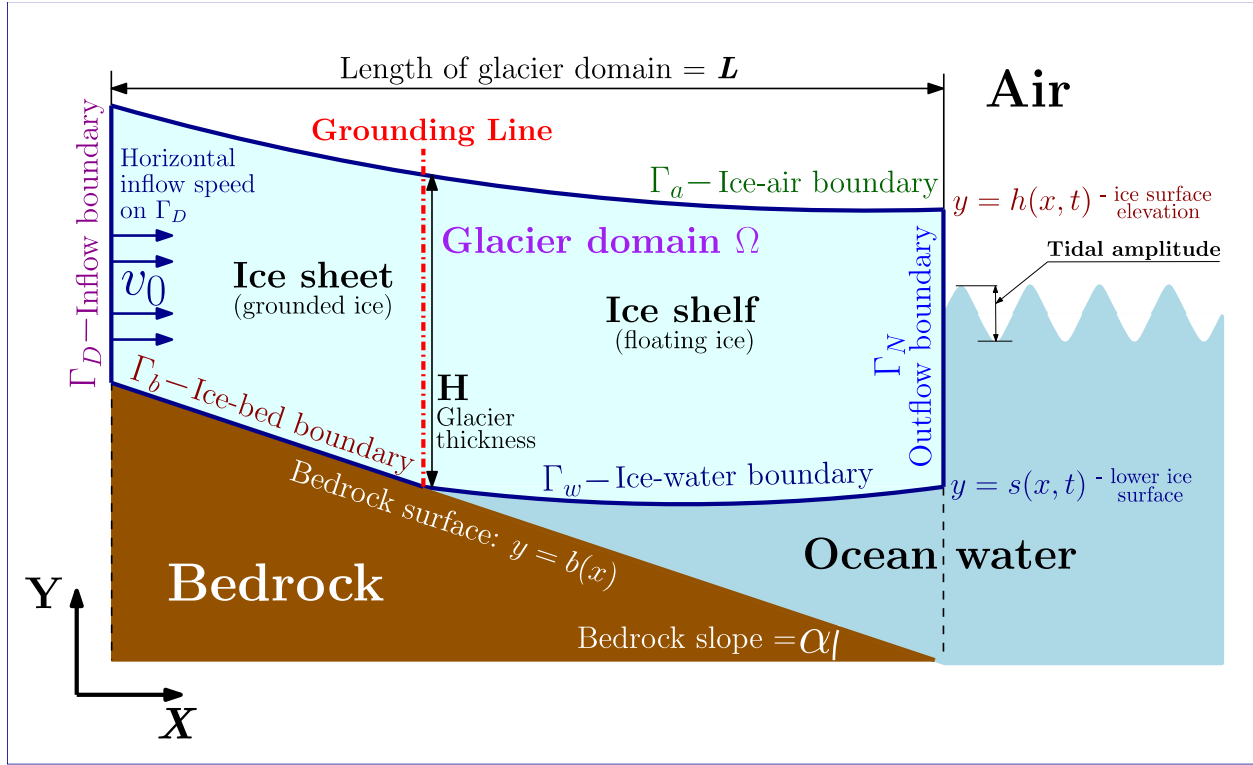


**Figure 4.** Model geometry for both viscous and viscoelastic problems, highlighting the ice domain  $\Omega$  boundaries, as defined in [Table 1](#).

### 2.1.3.3. Model formulation

Here, we describe the formulation of both models, which have the same domain and boundary conditions, but different governing equations. The summary of the notation mentioned here is provided in [Table 1](#).

Using the notation provided in [Table A1](#), we describe the formulation of both models, which have the same domain (see [Viscous and viscoelastic models](#)) and boundary conditions, but different governing equations.

#### 2.1.3.3.1. Governing equations

In both models, a glacier behaves as an incompressible non-Newtonian fluid, either viscous or viscoelastic. Incompressibility ~~implies-means~~ that the fluid density does not change during flow, which ~~is~~ mathematically ~~infers~~ ~~implies~~ zero divergence of the flow velocity  $\mathbf{v}$ :

$$\nabla \cdot \mathbf{v} = 0. \quad (6)$$

Both models are described by ~~the~~ Cauchy's first law of motion under quasi-static conditions, which provides the momentum conservation, ~~and is identified expressed~~ as:

$$\nabla \cdot \mathbf{T}(\mathbf{v}, p) + \rho_i \mathbf{g} = 0, \quad (7)$$

where  $\mathbf{T}$  is the Cauchy stress tensor,  $\rho_i$  is the ice density, and  $\mathbf{g}$  is ~~the vector of~~ gravitational acceleration ~~vector~~, which in the glacier reference system is identified as  $\mathbf{g} = g(0 \quad -1)^T$  with magnitude  $g$ .

The difference between the models becomes apparent when considering the constitutive law, ~~which defines~~ the physical nature of the models. The viscous model is described by the following equation:

$$\mathbf{T}(\mathbf{v}, p) = -p\mathbb{I} + 2\eta(\mathbf{v})\mathbf{D}, \quad (8)$$

where  $p$  is the ice pressure,  $\mathbb{I}$  is a second-order identity tensor,  $\eta(\mathbf{v})$  is a velocity-dependent ice viscosity, and  $\mathbf{D}$  is a strain rate tensor

$$\mathbf{D}(\mathbf{v}) = \frac{1}{2}[\nabla\mathbf{v} + (\nabla\mathbf{v})^T]. \quad (9)$$

Ice viscosity in the viscous model is identified via Glen's flow as

$$\eta(\mathbf{v}) = 2^{\frac{-1-n}{2n}} \cdot \sqrt[n]{A(|\mathbf{D}(\mathbf{v})|^2 + \delta)^{\frac{1-n}{2n}}}, \quad (10)$$

where  $n \geq 1$  is the stress exponent,  $A > 0$  is the ice softness, and  $\delta \ll 1$  is an infinitesimal numerical parameter, used to prevent numerical instability of the models at zero strain rate.

For the viscoelastic model, constitutive law (8) and the viscosity expression (10) are principally different. We consider the Maxwell model of viscoelasticity, which considers both viscous and elastic components. The Maxwell model assumes that deformation properties can be represented by a purely elastic spring and a purely viscous dashpot connected in series. Therefore, in the Maxwell model, a viscoelastic material behaves as a purely viscous flow under slow deformation (long timescale), while it exhibits elastic resistance to rapid deformations (short timescale). However, assince the simple Maxwell model describes small deformations, we apply the upper-convected Maxwell model instead, which includes some geometrical non-linearity. The constitutive relation for the viscoelastic model is identified as

$$\mathbf{T}(\mathbf{v}, p) = -p\mathbb{I} + \boldsymbol{\tau}, \quad (11)$$

where, compared to the purely viscous model (8), the strain rate tensor  $\mathbf{D}$  (equation (9)) is replaced with the deviatoric stress tensor  $\boldsymbol{\tau}$ , which is strain rate-dependent:

$$\boldsymbol{\tau} + \lambda \overset{\nabla}{\boldsymbol{\tau}} - 2\eta(\boldsymbol{\tau})\mathbf{D}(\mathbf{v}) = 0, \quad (12)$$

where  $\lambda = \frac{\eta(\boldsymbol{\tau})}{G}$  is the relaxation time with the shear modulus  $G$ . The viscoelastic model reduces to the viscous model described in Stubblefield et al. (2021) when  $\lambda = 0$ , while at infinitely big  $\lambda$ , the upper-convected Maxwell model reduces to a neo-Hookean elastic solid (Snoeijer et al., 2020). and the ice viscosity in equation (12) is

$$\eta(\boldsymbol{\tau}) = \frac{1}{2A|\boldsymbol{\tau}|^{n-1}}. \quad (13)$$

$\overset{\nabla}{\boldsymbol{\tau}}$  represents the upper-convected time derivative of  $\boldsymbol{\tau}$ :

$$\overset{\nabla}{\boldsymbol{\tau}} = \frac{D\boldsymbol{\tau}}{Dt} - (\nabla\mathbf{v})^T \cdot \boldsymbol{\tau} - \boldsymbol{\tau} \cdot \nabla\mathbf{v}, \quad (14)$$

where  $\frac{D\boldsymbol{\tau}}{Dt} = \frac{\partial\boldsymbol{\tau}}{\partial t} + \mathbf{v} \cdot \nabla\boldsymbol{\tau}$  is the material derivative of  $\boldsymbol{\tau}$ . The partial time derivative of  $\boldsymbol{\tau}$  on the current time step is calculated using the value from in the model through the previous time step, applying the -using-backward Euler approximation:

$$\frac{\partial\boldsymbol{\tau}(x, t)}{\partial t} = \frac{\boldsymbol{\tau}(x, t) - \boldsymbol{\tau}(x, t - \Delta t)}{\Delta t}. \quad (15)$$

### 2.1.2.3.3.2. Evolution of the lower boundary

The time evolution of the lower boundary  $y = s(x, t)$  is governed by the kinematic equation, which ~~states~~~~expresses~~ the fact that the surface moves with the ice flow ~~and under the assumption that there are~~ no mass changes at the lower surface, such as melting or freezing, the equation can be written as (Hirt and Nichols, 1981; Schoof, 2011)

$$\frac{\partial s}{\partial t} + v_x \frac{\partial s}{\partial x} = v_y, \quad (16)$$

where  $v_x$  and  $v_y$  are the components of the surface velocity vector  $\mathbf{v}|_s = (v_x, v_y)^T$ . Rewriting equation (16) in terms of the outward-pointing normal to the lower boundary  $\hat{\mathbf{n}}|_s = \frac{(\frac{\partial s}{\partial x}, -1)^T}{\sqrt{1 + (\frac{\partial s}{\partial x})^2}}$ , we get

$$\frac{\partial s}{\partial t} = -\mathbf{v} \cdot \hat{\mathbf{n}}|_s \cdot \sqrt{1 + \left(\frac{\partial s}{\partial x}\right)^2}. \quad (17)$$

As Since the solution of equation (17) is numerically unstable (Durand et al., 2009), we apply the backward Euler method to ~~get rid of~~~~remove~~ the instability. Denoting the approximate solution on  $k$ -th time step as  $s_*$ , such as  $s_* \equiv s(x, t_k)$ , and applying the backward Euler method to equation (17) under the assumption that  $\left(\frac{\partial s}{\partial x}\right)^2 \ll 1$ , we get

$$s_*(x, t_k) = s(x, t_k - \Delta t) - \Delta t \cdot v_n(x, s, t_k), \quad (18)$$

where  $\mathbf{v} \cdot \hat{\mathbf{n}}|_s$  was replaced with  $v_n$ . We assume that the ocean is hydrostatic and define  $p_w$  as the water pressure at the ice–water interface and  $p_w^0$  as the hydrostatic water pressure. If  $l$  is sea level, the hydrostatic water pressure at  $k$ -th time step is governed by the following equation:

$$p_w^0(x, s, t_k) = \bar{p}_w \rho_w g(l(t_k) - s_*(x, t_k)). \quad (19)$$

### 2.1.3.3.3.3. Boundary conditions

Identifying  $\hat{\mathbf{n}}(\mathbf{x})$  as a unit outward normal vector at some point  $\mathbf{x}$  of any domain boundary, we determine an orthogonal projection onto that boundary as a second-order tensor  $\mathbb{P}$ :

$$\mathbb{P} := \mathbb{I} - \hat{\mathbf{n}}(\mathbf{x}) \otimes \hat{\mathbf{n}}(\mathbf{x}), \quad (20)$$

where  $\otimes$  is the tensor product. Denoting  $\cdot$  as an inner product, we also define the projection of the Cauchy stress tensor  $\mathbf{T}$  as

$$T_n = -\hat{\mathbf{n}} \cdot \mathbf{T} \cdot \hat{\mathbf{n}}. \quad (21)$$

Both models use the same Dirichlet boundary conditions provided in Table 2, where  $v_0 > 0$  is the horizontal ice flow speed on the inflow boundary  $\Gamma_D$ .

**Table 2.** Models' boundary conditions

Boundary	Boundary condition	Physical meaning of a boundary condition	Equation number
$\Gamma_w$	$\mathbf{T} \cdot \hat{\mathbf{n}} = -p_w \hat{\mathbf{n}}$	Stress continuity at the ice–water boundary	(22)
$\Gamma_a$	$\mathbf{T} \cdot \hat{\mathbf{n}} = 0$	No stress at the ice–air boundary	(23)
$\Gamma_D$	$\begin{cases} v_x = v_0 \\ \mathbb{P} \mathbf{T} \hat{\mathbf{n}} = 0 \end{cases}$	On the inflow boundary the horizontal velocity is uniform and there is no vertical shear stress	(24)



$\Gamma_N$	$\mathbf{T} \cdot \hat{\mathbf{n}} = -\rho_i g(h - y)\hat{\mathbf{n}}$	<u>Cryostatic normal-stress condition on the outflow boundary</u>	(25)
$\Gamma_b$	$\mathbb{P}\mathbf{T}\hat{\mathbf{n}} + \phi(\mathbf{v})\mathbb{P}\mathbf{v} = 0^*$	<u>Sliding law on the ice-bed boundary</u>	(26)
$\Gamma_b$	$\begin{cases} T_n \geq p_w \\ v_n \leq 0 \\ (T_n - p_w)v_n = 0 \end{cases}$	<u>There are three possibilities for the normal stress and the normal velocity component on the ice-bed boundary:</u> <u>(1) The normal stress exceeds the water pressure (<math>T_n &gt; p_w</math>) and the ice is not lifted off of the bed (<math>v_n = 0</math>);</u> <u>(2) The normal stress equals the water pressure (<math>T_n = p_w</math>) and the ice is lifted from the bed (<math>v_n &lt; 0</math>);</u> <u>(3) The normal stress equals the water pressure (<math>T_n = p_w</math>), but the ice is not lifted from the bed (<math>v_n = 0</math>).</u>	(27)
* in equation (26), $\phi(\mathbf{v}) = C( \mathbb{P}\mathbf{v} ^2 + \delta)^{\frac{1-n}{2n}}$ is friction with friction coefficient $C$			

### 3.4. Viscoelastic model wWeak formulation

In this subsection, we provide the derivation of the viscoelastic model, while the viscous model is derived in (Stubblefield et al., 2021).

#### Mixed formulation

Let us define  $V$  as the velocity function space.  $K$  is a closed, convex subset of  $V$  such that

$$K = \{\mathbf{v} \in V: v_n|_{\Gamma_b} \leq 0 \text{ and } v_x|_{\Gamma_D} = v_0\} \quad (28)$$

Multiplying equation (7) by  $\mathbf{v} - \mathbf{u}$  (where  $\mathbf{u} \in K$  is an arbitrary test function), and integrating the expression over the glacier domain  $\Omega$ , in the indicial notation we will get:

$$\int_{\Omega} (v_k - u_k) T_{kj,j} dV + \int_{\Omega} \rho_i g_k (v_k - u_k) dV = 0. \quad (29)$$

Integrating the first integral in equation (29) by parts and applying the divergence theorem (Green's identity), we then apply equation (11) to one of the integrals and rewrite the resulting expression in tensor notation:

$$- \int_{\partial\Omega} \mathbf{T} \cdot \hat{\mathbf{n}} \cdot (\mathbf{v} - \mathbf{u}) da + \int_{\Omega} \{-p \nabla \cdot (\mathbf{v} - \mathbf{u}) + \boldsymbol{\tau} \cdot \nabla (\mathbf{v} - \mathbf{u}) - \rho_i g(\mathbf{v} - \mathbf{u})\} dV = 0. \quad (30)$$

Now we decompose  $\partial\Omega$  onto the compounding boundaries (see equation (2)) and consider the first integral in equation (30) over each boundary separately. Using equations (20), (21), and boundary condition (26) on  $\Gamma_b$ , after integration over  $\Gamma_b$  and taking into account that  $T_n \geq p_w$  on  $\Gamma_b$ , we derive that

$$- \int_{\Gamma_b} \mathbf{T} \cdot \hat{\mathbf{n}} \cdot (\mathbf{v} - \mathbf{u}) da \leq \int_{\Gamma_b} \alpha(\mathbf{v}) \cdot \mathbb{P}\mathbf{v} \cdot \mathbb{P}(\mathbf{v} - \mathbf{u}) da + \int_{\Gamma_b} p_w (v_n - u_n) da. \quad (31)$$

On  $\Gamma_w$ , from equation (22), we obtain the following expression:

$$- \int_{\Gamma_w} \mathbf{T} \cdot \hat{\mathbf{n}} \cdot (\mathbf{v} - \mathbf{u}) da = \int_{\Gamma_w} p_w (v_n - u_n) da. \quad (32)$$

On  $\Gamma_D$ , from equation (24), we have  $\mathbb{P}\mathbf{T}\hat{\mathbf{n}} = 0$ , thus, this boundary does not contribute to the integral  $\int_{\partial\Omega} \mathbf{T} \cdot \hat{\mathbf{n}} \cdot (\mathbf{v} - \mathbf{u}) da$ . On  $\Gamma_a$ , from equation (23), we have  $\mathbf{T} \cdot \hat{\mathbf{n}} = 0$ , thus, this the ice-air boundary does not

contribute to the integral  $\int_{\partial\Omega} \mathbf{T} \cdot \hat{\mathbf{n}} \cdot (\mathbf{v} - \mathbf{u}) da$  as well. On  $\Gamma_N$ , where from equation (25), we know  $\mathbf{T} \cdot \hat{\mathbf{n}} = -\rho_i g(h - y)\hat{\mathbf{n}}$ , which means that the contribution from the boundary to  $\int_{\partial\Omega} \mathbf{T} \cdot \hat{\mathbf{n}} \cdot (\mathbf{v} - \mathbf{u}) da$  will be

$$-\int_{\Gamma_N} \mathbf{T} \cdot \hat{\mathbf{n}} \cdot (\mathbf{v} - \mathbf{u}) da = \int_{\Gamma_N} \rho_i g(h - y)(v_n - u_n) da. \quad (33)$$

Substituting equations (31)–(33) to equation (30), replacing the union of  $\Gamma_w$  and  $\Gamma_b$  with  $\Gamma_s$  and replacing  $p_w$  with  $p_w = \rho_w g(l - s + \Delta t \cdot v_n)$ , which was derived from equations (18) and (19), we obtain

$$\begin{aligned} & \int_{\Omega} \{-p \nabla \cdot (\mathbf{v} - \mathbf{u}) + \boldsymbol{\tau} \cdot \nabla (\mathbf{v} - \mathbf{u}) - \rho_i g(\mathbf{v} - \mathbf{u})\} dV + \int_{\Gamma_N} \rho_i g(h - y)(v_n - u_n) da + \\ & + \int_{\Gamma_b} \alpha(\mathbf{v}) \cdot \mathbb{P} \mathbf{v} \cdot \mathbb{P}(\mathbf{v} - \mathbf{u}) da + \int_{\Gamma_s} \rho_w g(l - s + \Delta t \cdot v_n)(v_n - u_n) da \geq 0. \end{aligned} \quad (34)$$

We define  $Q$  as a function space for pressure ( $q \in Q$ ), and  $M$  as a function space for stress ( $\boldsymbol{\mu} \in M$ ). To shorten and simplify the notation, we introduce following functions:

$$F(\boldsymbol{\tau}, \mathbf{v}, \mathbf{u}) = \int_{\Omega} \boldsymbol{\tau} \cdot \nabla \mathbf{u} - \rho_i g \mathbf{u} dV + \int_{\Gamma_N} \rho_i g(h - y) u_n da + \int_{\Gamma_b} \alpha(\mathbf{v}) \cdot \mathbb{P} \mathbf{v} \cdot \mathbb{P} \mathbf{u} da \quad (35)$$

$$P(\mathbf{v}, \mathbf{u}) = \int_{\Gamma_s} \rho_w g(l - s + \Delta t \cdot v_n) u_n da \quad (36)$$

$$d_{\Omega}(\boldsymbol{\mu}, \boldsymbol{\tau}, \mathbf{v}) = \int_{\Omega} \boldsymbol{\mu} \left( \boldsymbol{\tau} + \frac{\eta}{G} \nabla \cdot \boldsymbol{\tau} - 2\eta D(\mathbf{v}) \right) dV \quad (37)$$

$$b_{\Omega}(q, \mathbf{v}) = \int_{\Omega} q \nabla \cdot \mathbf{v} dV \quad (38)$$

Writing inequality (34) in terms of equations (35)–(38), we obtain

$$\begin{cases} F(\boldsymbol{\tau}, \mathbf{v}, \mathbf{v} - \mathbf{u}) + P(\mathbf{v}, \mathbf{v} - \mathbf{u}) - b_{\Omega}(p, \mathbf{v} - \mathbf{u}) \geq 0 \\ d_{\Omega}(\boldsymbol{\mu}, \boldsymbol{\tau}, \mathbf{v}) = 0 \\ b_{\Omega}(q, \mathbf{v}) = 0 \end{cases} \quad (39)$$

By analogy with (Stubblefield et al., 2021), we replace the mixed formulation (39) with a penalty formulation

$$\begin{cases} F(\boldsymbol{\tau}, \mathbf{v}, \mathbf{u}) + P(\mathbf{v}, \mathbf{u}) - b_{\Omega}(p, \mathbf{u}) + \frac{\Pi'(\mathbf{v}, \mathbf{u})}{\epsilon} = 0 \\ d_{\Omega}(\boldsymbol{\mu}, \boldsymbol{\tau}, \mathbf{v}) = 0 \\ b_{\Omega}(q, \mathbf{v}) = 0 \end{cases} \quad (40)$$

Therefore, the penalized problem for the viscoelastic model is to find  $(\mathbf{v}, p, \boldsymbol{\tau}) \in V \times Q \times M$ , which satisfies the boundary conditions and the system (40).

### 2.2.3.5. Model setup

Both models consider a glacier as an incompressible, ~~and~~ non-Newtonian ice flow, sharing the same domain and restricted by identical boundary conditions. Using FEniCS, a freely available FEM Python package, ~~the both~~ models employ Taylor–Hood elements for velocity and pressure fields to solve ~~the a~~ corresponding variational problem on each time step by means of a Newton solver for nonlinear systems of equations. While Table S4 offers a brief comparison of the models, the primary distinction between the viscous and viscoelastic models lies in the incorporation of an elastic component, represented by Hooke’s law. The addition of the elastic component enables the viscoelastic

model to account for significant short-term glacier deformations, as provided by the application of the upper-convected Maxwell model of viscoelasticity. However, it also entails a substantial increase in computational resources required for a single model run (Table S4).

In the modeling framework, the bedrock slope ~~in the models~~ is set using the function

$$b(x) = -\frac{Ax}{L}, \quad (41)$$

where  $A$  is a variable parameter in meters that determines the bedrock inclination, and  $L$  is a glacier domain length, which is kept constant at 20 km for all model runs to ensure consistent results. The bed slope  $\alpha$  is determined as the tangent of the bedrock function  $b(x)$  and is measured

$$\alpha = \frac{A \cdot 100\%}{L}. \quad (42)$$

The grounding line position is defined based on the numerical tolerance  $\xi$ , set to 1 mm. If the computed position of a lower boundary mesh node  $s$  is  $\xi$  mm greater in the vertical direction than the bedrock, that node is classified as floating. Conversely, if a node position does not deviate from the bed by more than  $\xi$ , that node is classified as grounded. Schematically, the node classification can be described as:

$$\begin{cases} s - b \leq \xi \Rightarrow \text{grounded node} \\ s - b > \xi \Rightarrow \text{floating node} \end{cases} \quad (43)$$

Both viscous and viscoelastic models require bed slope, glacier thickness and ice inflow speed as input parameters. For one set of input parameters, the code solves the corresponding variational problem twice: first, for a calm ocean surface without tides to stabilize the glacier and approximate its shape to a more natural geometry than the initially specified one; and second, for the tidal situation where the grounding zone width is determined. As follows from the CATS2008 model (Padman et al., 2002), the investigated glaciers experience tidal fluctuations with an amplitude of approximately 1 m. Therefore, in the model, we employ sinusoidal-shaped tides with a 1 m amplitude and a half-day period  $P$ , which is typical for the investigated glaciers (Hibbins et al., 2010; Padman et al., 2018). Thus, the sea level, in a tidal case, changes with time as

$$l(t) = \frac{\rho_i}{\rho_w} H + \sin\left(\frac{2\pi t}{P}\right), \quad (44)$$

where  $H$  is the glacier thickness at the grounding line. However, although the glaciers exhibit tidal fluctuations with a 1 m amplitude (or 2 m peak-to-peak amplitude), the DInSAR interferograms used for model accuracy assessment show only ~1 m peak-to-peak amplitude (Column  $\Delta H$  in Table S6) due to the timing of the SAR image acquisition. To ensure a meaningful comparison between the measurements and the model results, the modeled grounding zones were calculated as the difference between grounding line positions sampled at the tidal levels corresponding to those captured by the DInSAR interferograms (Column  $H$  in Table S6).

We analyze ~~examined~~ the sensitivity of the models to mesh size by running ~~them~~ simulations with the same set of parameters, while ~~but~~ varying mesh sizes at the lower domain surface (from 10 m to 250 m with 10 m step) and, while keeping the upper domain mesh fixed at 250 m, the mesh size constant (250 m) at the upper surface of the glacier. Overall, ~~To determine establish~~ the most efficient mesh size, 200 grounding zone width values were obtained and analyzed (Figure S1). The accuracy of the viscoelastic model is more ~~significantly~~ affected by mesh size than ~~that~~ of the viscous model (see section ‘S2. Mesh sensitivity analysis’ in Supplementary materials). Since the empirically

determined manual grounding line mapping error can reach up to 200 m (Rignot et al., 2014; Ross et al., 2024), we conclude that For example, grounding zone width values for glaciers with thicknesses of 2.5 km and 1 km, both with an inflow speed of 100 m/year, converge to approximately 1.45 km for a mesh size of 250 m. However, at a mesh size of 10 m, these values were 0.96 km and 0.84 km, respectively (Figure S1 (d)). Comparing the dependences for the same slope of 5% for both models, we conclude that for glaciers with the same thickness, lower ice flow speed is more sensitive to the mesh size (red and black dots in Figure S1 (c) and (d)).

We empirically determined that the average accuracy of manual mapping is approximately 200 m, the mesh size impact remains within the confidence interval of manual mapping if therefore as long as the model outputs do not deviate by no more than 0.2 km from the asymptotic value of the grounding zone width, we can conclude that the mesh impact lies within the confidence interval of manual mapping. Significant The noticeable accuracy deterioration, exceeding 200 m, occurs at a mesh size of 210 m for the viscous model (Figure S1 (a)), and 200 m for the viscoelastic model (Figure S1 (d)). However, for in the viscoelastic model, we observe several step-like changes in the grounding zone width value, with the first noticeable shift takes occurring at a mesh size of 60 m (Figure S1 (b)). Therefore, to ensure the greatest possible modelling precision and maintain the consistency of the results, we have chosen a 50 m as the mesh size at the lower domain boundary for the following main analysis.

Model inputs were determined according to the MOS, TOT, and REN glaciers characteristics (Table S1 and Figure S4). The main analysis of the grounding zone evolution depending on physical representation (viscous or viscoelastic) and ice bed system parameters was carried out retaining a constant mesh size of 50 m and 250 m at the lower and upper domain boundaries, respectively, which was previously determined as the most efficient. Maintaining a consistent glacier domain length of 20 km for all model runs, various parameter tests were conducted, encompassing ice thicknesses of 1.0, 1.5, 2.0, and 2.5 km; horizontal ice inflow speeds of 100, 350, 600, and 800 m/year; and bedrock slopes of 5.0, 4.5, 4.0, 3.5, 3.0, 2.5, 2.0, 1.5, 1.0, 0.5, 0.1, and 0.05% (see Figure S2). Therefore, A total of 192 sets of initial parameters were investigated for each model, covering all possible combinations of the specified ice thickness, ice inflow speed, and bedrock slope values listed in Figure S3. For each parameter set, both the viscous and viscoelastic models were initially run for a duration of two months within the model's time frame, assuming a stationary ocean with no tides to allow the model to reach stability. Subsequently, the models were run over a 7-day period with tides incorporated. Since the models utilize sinusoidal waves for tide simulation, the still water scenario corresponds to the zero-tide situation in the tidal problem. To justify these parameters we run multiple tests, ensuring that the grounding zone width does not change whether a zero-tide, high-tide (+1 m), or low-tide (-1 m) was chosen to initiate the tidal model run. In the still water scenario, the water level corresponds to the low tide situation in the tidal problem. The choice of a one-week time limit for the tidal problem allows the model to adapt to tidal impacts and enhances results accuracy. In most tidal model simulations runs, the grounding zone width slightly increases within the first 3 to 5 days with each tide while the models adapt and stabilizes afterward. Several test runs, lasting up to 14 days within the modeling framework, were conducted to estimate the impact of the grounding zone width increase during the initial days. These test runs show that the grounding zone width stops changing after the first five days and remains stable, showing no significant variations afterwards. The initial increase occurs gradually, with the initial grounding zone width being, on average, 80% of the final stabilized width, which is reached after 5 days. Therefore,



The resulting grounding zone width value for each model run is determined as the average of the grounding zone width values simulated for days six and seven for the last two days.

The source code of the viscous model, developed by Stubblefield et al. (2021), was used as a basis of the viscoelastic model (see Code and Data availability). Necessary adjustments to the mesh size and glacier parameters for both publicly available source codes were made accordingly. Consequently, a total of 1,168 model runs were performed while conducting the research: 400 runs for the mesh sensitivity analysis and 768 runs for the main analysis, which includes the grounding zone width dependence analysis from the main glacier parameters for both models. As for the grounding line generation two model runs are required, 584 grounding zone values were obtained: 200 for the mesh sensitivity analysis and 384 for the main analysis. In total, these code runs required about 1400 hours (~58 days) of continuous computations.

## 4. Results

### 4.1. Measured glacier parameters

A summary of the glacier parameters, including ice flow speed, ice thickness, bed slope and grounding zone width, measured along the 69 selected profiles, is provided in Table S1. TOT exhibits the shallowest average bed slope among the glaciers of interest, measuring  $1.2 \pm 0.1$  % on average. The glacier has an average grounding zone width of  $4.1 \pm 0.4$  km and a mean thickness of  $2.2 \pm 0.1$  km, making it the fastest one among the three glaciers with an average speed of  $647 \pm 77$  m/year. In contrast, REN is the thinnest and slowest among the three, with a mean thickness of  $1.1 \pm 0.2$  km and a flow speed of  $172 \pm 24$  m/year. It also features the smallest average grounding zone width of  $2.3 \pm 0.4$  km and a rising inland bed with an average rate of  $1.1 \pm 0.2$  %. MU, characterized by the smallest mean grounding zone of  $2.1 \pm 0.4$  km, also has the steepest average bed slope of  $2.2 \pm 0.2$  %. With an average thickness of  $2.2 \pm 0.1$  km, the glacier maintains a mean ice flow speed of  $335 \pm 20$  %.

The DInSAR-derived grounding zones exhibit an inverse relationship with bedrock slopes (Figure S1): larger grounding zones correspond to shallower slopes, while narrower grounding zones are found over steeper slopes. The correlation between bed slope ( $\alpha$ ) and grounding zone width (GZ), both for each glacier individually and for all three glaciers combined, can be modeled by an inverse power law function  $\alpha = a \cdot GZ^b + c$ , where the term ‘inverse’ indicates that the fitting coefficient  $b$  is negative. Based on the standard error of regression, we conclude that REN and TOT closely follow this inverse power law pattern, while MU introduces some variability, particularly due to its wide grounding zones exceeding 6 km. The standard error of 0.4 km, calculated when considering all three glaciers together, suggests that the overall relationship between grounding zone width and bedrock slope aligns well with the inverse power law model.

Additionally, Li et al. (2023) mentions that both ICESat laser altimetry and Sentinel-1a/b three-image DInSAR interferometry failed to delineate main trunk of TOT glacier and the central part of the MU main trunk due to the fast ice flow in these regions. On the contrary, the four-image CSK DInSAR technique utilized in this study allowed us to map grounding lines even over these fast-flowing areas. Li et al. (2023) estimated the average grounding line retreat between 1996 and 2020 as  $3.51 \pm 0.49$  km for the southern lobe of the TOT main trunk, and as 13.85 km and 9.37 km for the western and eastern flanks of the MU main trunk, respectively. As, according to Li et al. (2023), it is impossible

to determine the magnitude of tidally induced grounding line migrations in 1996 from the historic grounding line dataset (Rignot et al., 2016), we assume the 1996 grounding line position as the average position between high and low tides. To calculate the long-term retreat, we estimate the distance from the historic grounding line to the center of the DInSAR-derived grounding zones for each glacier of interest. As a result, for MU, between 1996 and 2021, we detect an average retreat of the main trunk of  $9 \pm 2$  km, with  $18 \pm 1$  km retreat at the western flank,  $6.7 \pm 0.6$  km retreat at the central part of the main trunk, and  $4.2 \pm 0.6$  km retreat at the eastern flank. ~~Therefore~~Thus, the western flank demonstrates the highest retreat rate of  $690 \pm 40$  m/year, while the average glacier retreat rate over this period was  $340 \pm 80$  m/year. For TOT, between 1996 and 2020, we observe an average retreat of the main trunk of  $9 \pm 3$  km with  $13.9 \pm 0.1$  km retreat at the western flank,  $17 \pm 1$  km retreat at the central part of the main trunk, and  $5.2 \pm 0.3$  km retreat at the eastern flank. Therefore, while the average rate of TOT retreat between 1996 and 2020 was  $360 \pm 120$  m/year, the central part of the main trunk retreated as fast as  $680 \pm 40$  m/year. ~~Meanwhile~~In the meantime, the position of the REN grounding line at the main trunk did not change between 2000 and 2020, which indicates ~~signifies~~ the stability of the glacier over the past 20 years.

## **4.2. Modeled Glaciers Parameters**

### **2.2.1.4.2.1. The role of glacier thickness**

## **3. Discussion**

### **3.1. Modeled tide-induced grounding zone dependence from ice-bed system parameters**

~~A total of 384 grounding zone width values were generated utilizing all possible combinations of selected ice bed system parameters (Figure S2), while maintaining constant mesh sizes of 250 m and 50 m at the upper and lower glacier surfaces, respectively. These grounding zones are illustrated in Figure 5~~ shows the modeled grounding zone widths as a function of ice thickness, where they are grouped by the bedrock slope and color-coded based on inflow speed for each model. In both the viscous and viscoelastic models, the Figure 5 ~~Figure 3 shows the dependence of the grounding zone width on the glacier thickness for each bed slope, with the outputs color-coded based on the inflow speed. The relationship between modeled grounding zone width (GZ) exhibits a linear relationship with glacier and ice thickness (H). Using the modeled grounding zone width values and approximating them with for each inflow speed and bed slope can be approximated by a linear function  $GZ = a \cdot H + b$ , we estimate coefficients of determination ( $R^2$  values), where coefficients  $a$  and  $b$  are unique for each model formulation, bed slope, and ice inflow speed. The approximation equations with corresponding coefficients of determination ( $R^2$  values) are provided in Table S2~~ shows that, where  $R^2$  ranges from 0.90 to 1.00 for the viscous model and from 0.87 to 1.00 for the viscoelastic model, which highlights showing a high linearity of the grounding zone dependence on the glacier thickness for any-all bedrock slopes if ice speed is constant. The main difference between the two models lies in the magnitude of the modeled grounding zone width as a function of glacier thickness over varying bed slopes. For example, for a bed slope of 0.05% and a glacier velocity of 800 m/yr, the viscous model predicts a grounding zone width of approximately 16 km, which is about twice the width estimated by the viscoelastic model (Figure 5).

In both models, shallower bed slopes increase the sensitivity of grounding zone width to changes in glacier thickness (Table S3). However, the viscous model is more sensitive to ice thickening compared to the viscoelastic model. In the

viscous model, for slopes between 1.0% and 5.0%, the grounding zone width increases by less than 1 km as glacier thickness increases from 1 km to 2.5 km. In contrast, on a 0.05% bed slope, the grounding zone expands by 6.1 km due to the same increase in glacier thickness. The viscoelastic model, however, predicts a more moderate increase: for a 0.05% bed slope, ice thickening from 1 km to 2.5 km results in a 2.5 km widening of the grounding zone (Table S3). Thus, the viscous model predicts a more pronounced response to changes in bed slope compared to the viscoelastic model.

#### 4.2.2. Influence of glacier velocity on grounding zone width

Our simulations enable us to characterize the behavior of the grounding zone width as a function of varying glacier velocities. Both models indicate that for slopes between 0.5% and 5.0%, an increase in ice inflow speed by 700 m/year results in up to a 10% expansion in grounding zone width (Figure 5). The most pronounced effect of velocity changes on grounding zone width occurs at shallower slopes of 0.1% and 0.05%. For these slopes, an increase in ice velocity from 100 m/year to 800 m/year can result in up to a 60% increase in grounding zone width in both the viscous and viscoelastic models (Figure 5). Additionally, both models show that at shallow slopes, glaciers with higher flow velocities are characterized by larger grounding zones for the same ice thickness. This indicates that for nearly flat bedrocks, a grounding zone width is more affected by variations in ice thickness for faster-flowing glaciers.

The linear approximation  $GZ = a \cdot H + b$  of the values shown in Figure 3, performed separately based on the bed slope for each inflow speed, facilitates tracking the evolution of the grounding zone dependence on ice flow speed as the bed slope increases. Denoting  $a_{100}$ ,  $a_{350}$ ,  $a_{600}$ ,  $a_{800}$  as slope coefficients for ice inflow speeds of 100, 350, 600, and 800 m/year, respectively, reveals the following evolution of their relative magnitudes:  $a_{100} > a_{350} > a_{600} > a_{800}$  for bed slope  $5.0\% \geq \alpha \geq 3.0\%$  and  $\alpha = 0.5\%$ ,  $a_{100} > a_{600} > a_{350} > a_{800}$  for bed slope  $2.5\% \geq \alpha \geq 1.5\%$ ,  $a_{600} > a_{100} > a_{800} > a_{350}$  for bed slope  $\alpha = 1.0\%$ ,  $a_{350} > a_{100} > a_{600} > a_{800}$  for bed slope  $\alpha = 0.1\%$ , and  $a_{800} > a_{600} > a_{350} > a_{100}$  for bed slope  $\alpha = 0.05\%$  for the viscous model (see Table S2 and Figure 3). Analogously, for the viscoelastic model, the slope coefficients demonstrate the following pattern:  $a_{100} > a_{350} \geq a_{600} > a_{800}$  for bed slope  $5.0\% \geq \alpha \geq 4.5\%$  and  $2.5\% \geq \alpha \geq 2.0\%$ ,  $a_{350} > a_{100} > a_{600} \geq a_{800}$  for bed slope  $4.0\% \geq \alpha \geq 3.5\%$  and  $\alpha = 1.5\%$ ,  $a_{100} > a_{600} > a_{350} > a_{800}$  for bed slope  $\alpha = 3.0\%$ ,  $a_{100} > a_{350} > a_{800} > a_{600}$  for bed slope  $\alpha = 1.0\%$ ,  $a_{600} > a_{350} > a_{800} > a_{100}$  for bed slope  $\alpha = 0.5\%$ ,  $a_{800} > a_{600} > a_{350} > a_{100}$  for bed slope  $0.1\% \geq \alpha \geq 0.05\%$ . Therefore, at steeper slopes, both models exhibit the same ratio of slope coefficients, namely,  $a_{100} > a_{600} > a_{350} > a_{800}$ , which changes to the reverse ratio at shallower slopes:  $a_{800} > a_{600} > a_{350} > a_{100}$ . This indicates that at steeper slopes, a grounding zone is more sensitive to changes in glacier thickness if the ice flow is slow, while for almost flat bedrocks, a grounding zone width is more affected by variations in ice thickness of faster-flowing glaciers.

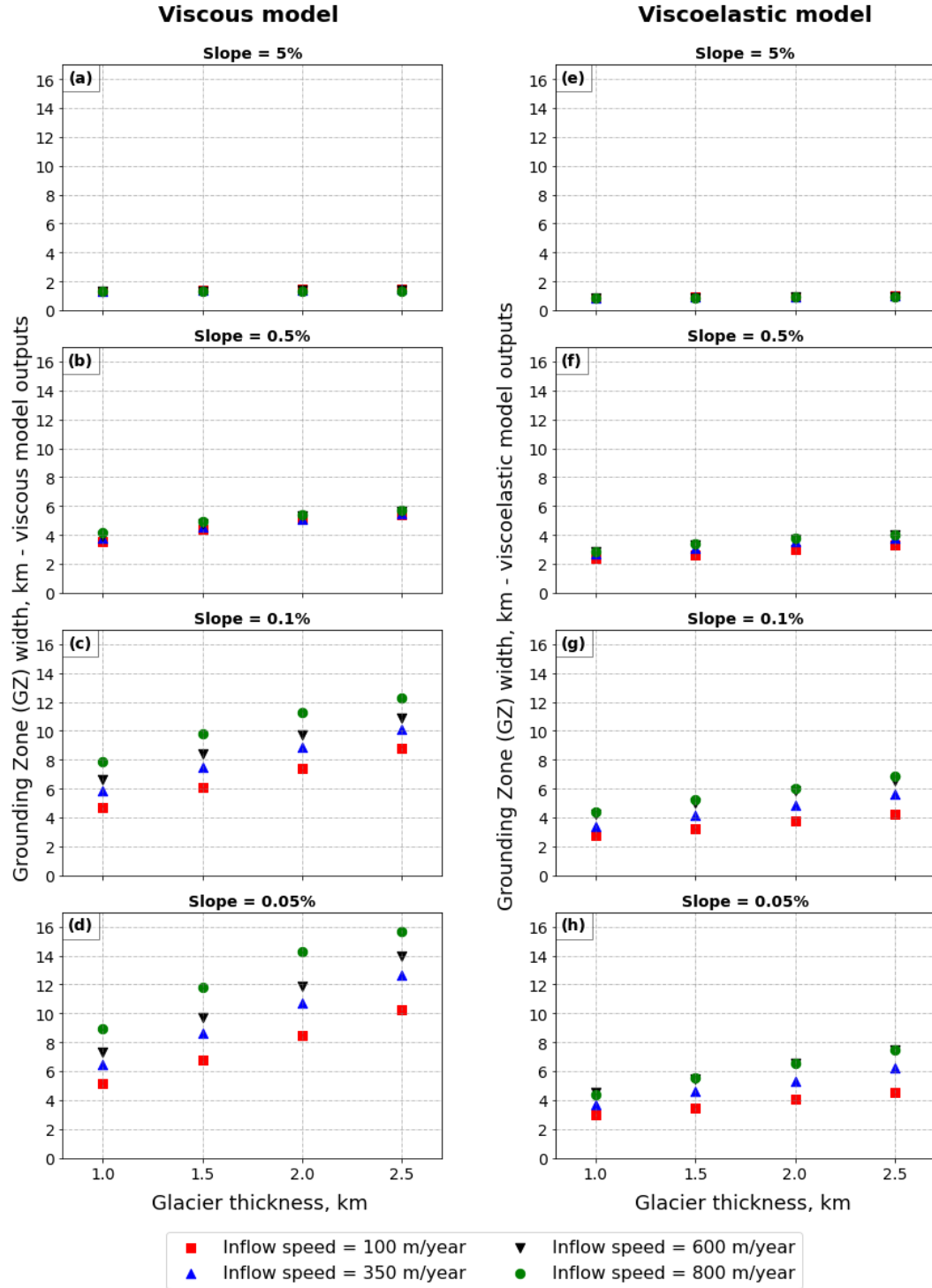


**Figure 5.** Dependence of the grounding zone width from the glacier thickness for all considered inflow speeds of 100, 350, 600, and 800 m/year and bed slopes of 5, 0.5, 0.1, and 0.05% for both viscous (subplots (a)–(d)) and viscoelastic models (subplots (e)–(h)). Subplots (a)–(d) correspond to the viscous model; subplots (e)–(h) correspond to the viscoelastic model. Corresponding bed slope is written above each subplot, the x-axis of each subplot shows the glacier thickness in meterskm, while the y-axis shows the evolution of the grounding zone as the glacier



becomes thicker. Each subplot contains four sets of values, colored based on the inflow speed ~~used as a model input at a corresponding model run.~~

### 4.2.3. Impact of bed slope on grounding zone extent

Figure 6 (a) and Figure 6 (b) present the grounding zone width obtained for the viscous and viscoelastic models, respectively, where the results for different inflow speeds are averaged by glacier thickness. Horizontal lines associated with the modeled grounding zones, in Figure 6 (a) and Figure 6 (b), represent the range of modeled grounding zone width values as a function of ice speed for a given ice thickness. In both models, grounding zone width increases as the bedrock slope decreases, indicating that the relationship between glacier bed slope and grounding zone width follows an inverse power law (dotted lines in Figure 6 (a) and (b)). The steepest rate of decay is observed for the thinnest glaciers (1 km), which are associated with the narrowest grounding zones. The shallowest power law applies to the thickest glaciers (2.5 km), resulting in the widest grounding zones.

The grounding zone width values from the viscoelastic model ( $GZ_{VE}$ ) plotted against the outputs from the viscous model ( $GZ_V$ ) reveal a linear relationship:  $GZ_{VE} = 0.49 \cdot GZ_V + 0.47$ , with a coefficient of determination ( $R^2$ ) of 0.97 (Figure 6 (d)). Consequently, for any combination of bedrock slope, glacier thickness, and ice inflow speed, the grounding zone width obtained from the viscoelastic model is nearly half that of the grounding zone width calculated by the viscous model on shorter time scales.

### 4.3. Evaluation of model performance using DInSAR grounding zone measurements

Figure 6 (c) shows the superimposed outputs of the viscous and viscoelastic models alongside the DInSAR grounding zone measurements over MU, TOT, and REN glaciers overlaid on the outputs of both viscous and viscoelastic models. The dashed lines, outlining the models' domains, are shown in Figure 6 (a), (b), and (c), while their equations are provided in Figure 6 (a) and (b) with the corresponding standard error of regression ( $S$ ). The models' domains, shown in Figure 6 (c) in pink for the viscous model and in green for the viscoelastic model, were determined using the function  $\alpha = a \cdot GZ^b + c$ , where  $\alpha$  is the input bed slope,  $GZ$  is the modeled grounding zone, and  $a$ ,  $b$ , and  $c$  are the fitting coefficients obtained through least-squares fit of the model outputs in Figure 6 (a) and (b). For each model, the upper domain boundary was established by fitting the largest modeled grounding zone outputs for each slope, while the lower domain boundary was defined by fitting the smallest modeled grounding zone outputs for each slope. The standard error of regression ( $S$ ) is 0.12 and 0.16 for the upper and lower viscous domain boundaries, respectively, and 0.08 and 0.07 for the upper and lower viscoelastic domain boundaries, respectively. Therefore, the power law function  $\alpha = a \cdot GZ^b + c$  accurately represents not only the DInSAR-derived grounding zone measurements (Figure S1), but also the models' output ranges.

To determine the models' accuracy, we measure the percentage of DInSAR measurements that fall inside the domain of a corresponding model. Disregarding the measurements error bars, only ~29%, ~0%, and ~9% of TOT's, REN's, and MU's measurements, respectively, fall into the viscous model's domain. Meanwhile, ~88% of TOT, 90% of REN, and ~82% of MU measurements (not accounting for the measurements errors) are successfully accommodated by the viscoelastic model. When including measurement errors, the model performance improves (Table S5). For the viscous model, the percentage of successfully modeled measurements increases from ~29% to ~65% for TOT, from ~0% to

~47% for REN, and from ~9% to ~82% for MU. For the viscoelastic model, this performance improvement is evident in the following notable expansions: from ~90% to ~100% for REN, from ~82% to ~100% for MU and remains consistently at ~88% for TOT. Overall, considering all three glaciers and all profiles, the viscous model achieves approximately 12% accuracy without measurement error bars and 70% accuracy with them, while the viscoelastic model achieves around 86% accuracy without error bars and 97% accuracy with them. Therefore, considering all the profiles and the measurement error bars, the viscoelastic model outperforms the viscous model by ~28%. However, without error bars, the viscoelastic model outperforms the viscous model by ~74%. This finding underscores the critical importance of incorporating the elastic component in Navier-Stokes-based fluid glacier formulations for representing tidally induced grounding zone migrations.

Additionally, ~~Figure 5~~ Figure 3 and Table S2 also show that the linear dependence  $GZ = a \cdot H + b$  becomes steeper as the bed slope decreases, which, in terms the slope coefficient  $a$ , means that the coefficient's magnitude increases as the bedrock becomes shallower. We conducted further analysis using the data from ~~Figure 5~~ Figure 3 by subtracting the grounding zone widths corresponding to the thickest and the thinnest glaciers ( $\Delta GZ$ ) for each bed slope and ice flow speed. While this analysis aimed to assess the impact of glacier thickness on the grounding zone for different bed slopes, Table S3 confirms the previous conclusion that the grounding zone at steep bed slopes is more sensitive to lower flow speeds, as evidenced by the descending order of  $\Delta GZ$  values in the column corresponding to 5.0% bed slopes for both models. Conversely, both models exhibit an ascending order of  $\Delta GZ$  values in 0.05% column, indicating a higher sensitivity of grounding zone to ice thickness for faster flowing glaciers.

The  $\Delta GZ$  values, averaged between those corresponding to different flow speeds for each bed slope and denoted as 'Mean' in Table S3, increase as the bed slope decreases. This pattern is observed for both models, with the mean difference values being larger for the viscous model. At a 5.0% bed slope, the difference in mean  $\Delta GZ$  does not exceed 10 meters: 98 m versus 105 m for the viscous and viscoelastic models, respectively. The difference in  $\Delta GZ$  remains similar between 5.0% and 1.0% bed slopes, while  $\Delta GZ$  for the viscoelastic model is less than two times greater than  $\Delta GZ$  for the viscous model. However, at a 0.5% bed slope,  $\Delta GZ$  for the viscous model becomes greater than  $\Delta GZ$  for the viscoelastic model. At a bed slope of 0.05%,  $\Delta GZ$  for the viscous model is almost 2.4 times greater than that for the viscoelastic model: 6130 m versus 2543 m for viscous and viscoelastic models, respectively. Moreover, the viscous model predicts a ~62 times enlargement of  $\Delta GZ$  if the bed slope changes from 5.0% to 0.05%, while the viscoelastic model forecasts a ~24 times enlargement of  $\Delta GZ$  for the same slope change.

### 3.2. — Model validation with DInSAR grounding zone measurements

In addition to the grounding zone, along each of 80 profiles we calculated the average values of bedrock slope, glacier thickness, and flow speed. While grounding zones were used to verify the models' performances, bed slopes, ice thicknesses, and flow speeds were used as input parameters. Therefore, as every profile is characterized by three input measurements, a total of 240 input measurements were performed. We test the models using bed slopes varying from 5% to 0.05% with ice thicknesses ranging from 1.0 to 2.5 km, and ice inflow speeds from 100 to 800 m/year. This choice of model input parameters ranges ensures that ~97% of the input measurements, accounting for the corresponding measurement errors, fall within the specified ranges (Table S1).

The relative distribution of input measurements is shown in Figure S3. All the ice flow measurements (Figure S3) fall between 100 m/year and 800 m/year, with REN's speed measurements being smaller than 200 m/year, MU's values ranging between 150 and 400 m/year, and TOT's speeds exceeding 500 m/year. REN does not have slopes lower than 0.8%, while MU and TOT have shallower slopes. Histogram (j) in Figure S3 shows high density of measurements clustered between 0% and 0.2% bedrock slopes if not accounting for the measurement errors. Due to computational limitations, we are unable to model bedrock slopes shallower than 0.05%. However, considering bed slopes associated errors (Figure 4), the minimum bed slope of 0.05% ensures that all the measurements along shallow beds fall into the modeled range of bed slopes (from 0.05% to 5%). Three bed slope measurements are greater than 5.0%, with two belonging to MU (profiles 27 and 28 in Table S1) and one to REN (profile 0). The Interquartile Range (IQR) method of outlier removal, which classifies a data point as an outlier if it exceeds the 25<sup>th</sup> percentile of the dataset by more than 1.5 · IQR or falls behind the 75<sup>th</sup> percentile by more than 1.5 · IQR, detected these three measurements as outliers (empty dots in box plot E1 in Figure S3). Only four thickness measurements, all belonging to REN (profiles 0, 1, 2, and 3), are less than 1 km (histograms (h) and (k) in Figure S3), and were classified by the IQR-based method as outliers as well (empty dots in box plot (n) in Figure S3). These seven measurements (four for ice thickness and three for bed slope), determined by the IQR-based method as outliers belong to six profiles: four for REN (profiles 0, 1, 2, and 3), and two for MU (profiles 27, 28). We assess the models' capabilities to model DInSAR observed grounding zones including and excluding these six profiles (Figure 4d).

Figure 4 provides the comparison of the viscous and viscoelastic models with each other and with the remote sensing observations over MU, TOT, and REN glaciers. Figure 4 (a) and Figure 4 (b) present the grounding zone width obtained for the viscous and viscoelastic models, respectively, where the results for different inflow speeds are averaged by glacier thickness. Error bars in Figure 4 (a) and Figure 4 (b) represent critical grounding zone width values, which are dependent on ice speed for a given ice thickness. The grounding zone width for both models increases as the bedrock slope decreases. The steepest dependence is observed for the smallest tested glacier thickness (1 km), while the shallowest dependence, resulting in the largest grounding zone width values, characterizes the thickest glaciers (2.5 km). The grounding zone width values of the viscoelastic model ( $GZ_{VE}$ ) plotted against the viscous model's outputs  $GZ_V$ , as shown in Figure 4 (d), exhibit a linear relationship:  $GZ_{VE} = 0.49 \cdot GZ_V + 0.47$ , with a coefficient of determination ( $R^2$ ) of 0.97. Consequently, for any combination of bedrock slope, glacier thickness, and ice inflow speed, the grounding zone width obtained from the viscoelastic model is nearly half that of the grounding zone width calculated by the viscous model on shorter time scales.

As each profile is characterized by a specific slope, thickness, and speed measurement, the measurements falling outside the chosen ranges pertain to six profiles: four for REN (profiles 0, 1, 2, and 3), and two for MU (profiles 27 and 28). These profiles are labeled as 'extra' profiles in Table S2. We performed the assessment of the models' capabilities to replicate DInSAR observed grounding zones, both including and excluding these 'extra' profiles. Figure 4C indicates the superimposed outputs of the viscous and viscoelastic models alongside the DInSAR grounding zone measurements overlaid on the modeling results, where empty circular markers correspond to the grounding zones extracted along the 'extra' profiles.

Considering all 80 profiles and disregarding the measurements' error bars,  $\sim 41\%$ ,  $\sim 0\%$ , and  $\sim 14\%$  of TOT's, REN's, and MU's measurements, respectively, fall into the viscous model's domain. Meanwhile,  $\sim 88\%$  of TOT's measurements,  $100\%$  of REN's measurements, and  $\sim 71\%$  of MU's measurements, all without considering the error bars, are successfully accommodated by the viscoelastic model. When including the error bars in consideration, the performance of the models significantly improves. For the viscous model, the percentage of successfully modeled measurements increases from  $\sim 41\%$  to  $\sim 65\%$  for TOT, from  $\sim 0\%$  to  $\sim 26\%$  for REN, and from  $\sim 14\%$  to  $\sim 39\%$  for MU. For the viscoelastic model, this performance improvement is evident in the following notable expansions: from  $\sim 88\%$  to  $\sim 100\%$  for TOT, from  $\sim 71\%$  to  $\sim 84\%$  for MU and remains consistently at  $100\%$  for REN. Excluding the 'extra' profiles,  $\sim 29\%$  versus  $\sim 57\%$  of the TOT's measurements fall within the domain of the viscous model when disregarding and considering the measurements' error bars, respectively. Analogously, for the viscous model,  $\sim 0\%$  turns into  $\sim 33\%$  for REN, and  $\sim 13\%$  transforms into  $\sim 47\%$  for MU when taking the measurements' error bars into account. Disregarding the 'extra' profiles, the difference in the viscoelastic model's performance, when ignoring and considering the error bars, changes from  $\sim 86\%$  to  $\sim 100\%$  for TOT, increases from  $\sim 76\%$  to  $\sim 87\%$  for MU, and remains unchanged at  $100\%$  for REN.

Determining model's accuracy as the percentage of DInSAR measurements that fall inside the domain of a corresponding model, for the viscoelastic model, REN consistently demonstrates  $100\%$  accuracy regardless of whether the 'extra' profiles are considered, and whether error bars are included or not. For TOT, the accuracy remains at  $100\%$  when the error bars are included, with or without the 'extra' profiles, while without the measurements' error bars, the 'extra' profiles improve accuracy by only  $\sim 2\%$ . For MU, the inclusion of the 'extra' profiles results in a  $\sim 5\%$  accuracy increase without the error bars, and a  $\sim 3\%$  increase with the error bars. Conversely, for the viscous model, the inclusion of the 'extra' profiles improves the accuracy only for TOT: without the 'extra' profiles, the accuracy improves by  $\sim 8\%$  and  $\sim 12\%$  with and without the error bars, respectively. However, the accuracy of the viscous model decreases by  $\sim 6\%$  and  $\sim 8\%$  for REN and TOT, respectively, when the 'extra' profiles are removed and the measurements' error bars are considered. Thus, discarding the 'extra' profiles does not significantly enhance the models' performances and may even reduce the percentage of successfully modeled measurements in some cases.

Overall, considering all three glaciers together and accounting for all 80 profiles, the viscous model achieves  $\sim 16\%$  or  $\sim 41\%$  accuracy without or with the measurements error bars, respectively, while the viscoelastic model achieves  $\sim 81\%$  or  $\sim 91\%$  accuracy without or with the measurements error bars, respectively. Excluding the 'extra' profiles, the accuracy of the viscous model improves from  $\sim 13\%$  to  $\sim 46\%$  when the measurements' error bars are considered, while the accuracy of the viscoelastic model changes from  $\sim 84\%$  to  $\sim 93\%$  when the measurements' error bars are taken into account. Therefore, excluding the 'extra' profiles and considering error bars, the viscoelastic model outperforms the viscous model by  $\sim 47\%$ . However, without error bars, the viscoelastic model outperforms the viscous model by  $\sim 71\%$ . This finding underscores the critical importance of incorporating the elastic component in Stokes-based fluid glacier formulations.

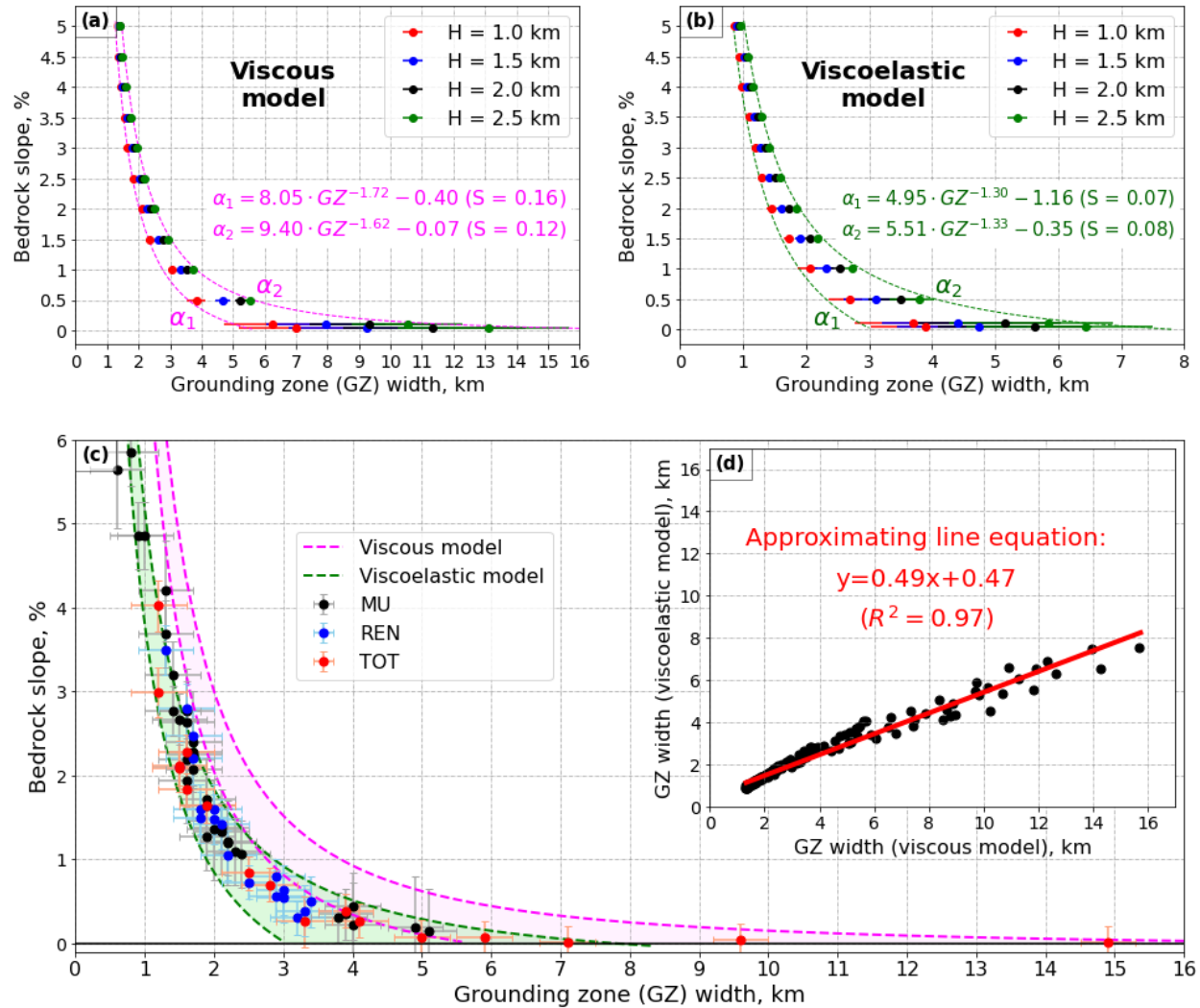


**Figure 6.** Modeling results of (a) viscous and (b) viscoelastic models, averaged by the thickness values, with pink and green outlines corresponding to error bars, representing the distance between the averaged grounding zone width for given thickness and maximum/minimum grounding zone (GZ) values for this the same thickness but different inflow speed values; (c) comparison of the modelling results (pink and green areas) with the DInSAR grounding zone measurements, where empty markers show grounding zones obtained along ‘extra’ profiles from Table S2; (d) correlation plot of the modelling results. Dotted green and pink lines are the same on subplots (a), (b), and (c), while their equations are provided in subplots (a) and (b).

## 5. Discussion

### 5.1. Grounding zone width dependence as a function of input parameters

Our models show that the grounding zone widens as the bed slope becomes shallower, following a non-linear relationship. This model-derived finding which is consistent with our data as well as with previous observational studies (Chen et al., 2023; Milillo et al., 2017, 2019, 2022). Furthermore Secondly, both our models and data indicate that for a given bed slope, the grounding zone is wider grounding zones are found where glaciers are for a thicker



glacier, with a linear relationship observed which is not only evident from the modeling results but is also supported by the DInSAR measurements (Figure 7 (a) and (b)). This observation can be associated with the increase of the flexural wavelength of ice when its thickness increases (Freer et al., 2023). For thicker ice, the same tidal amplitude affects a larger horizontal distance, leading to a broader grounding zone. This effect is more pronounced on shallow slopes, where the tidal amplitude influences a larger area. Glacier velocity significantly impacts grounding zone width for bed slopes below 0.1% due to the increase in elastic stresses with faster glacier flow (Christmann et al., 2021). As a result, the elastic stress of fast-flowing glaciers on shallow slopes is higher than that of slower-moving glaciers, making the former more sensitive to thickness changes and confirming our observations (Figure 7 (c)). Considering DInSAR measurements characterized by bed slopes ranging from 0.1% to 0.5% and ice flow speeds ranging from 100 to 350 m/year and overlaying them with modelling results obtained for the same range of bed slopes and flow speeds, we obtain a linear correlation between glacier thickness and grounding zone width (Figure 7 Figure 5 a). Analogously, in Figure 7 Figure 5 b, a similar linear relationship between glacier thickness and grounding zone is observed for the same range of glacier flow speeds and bed slopes ranging from 1.6% to 2.5%. The range of slopes was increased compared to Figure 7 Figure 5 a as the grounding zone sensitivity to variations in bed slopes decreases when bed becomes steeper, according to the first conclusion we made. Lastly, it can be concluded from the modeled grounding zones that on steep bed slopes, the grounding zone is more responsive to changes in glacier thickness when ice flow is slow; on shallow (mostly flat) bedrocks, the grounding zone is more sensitive to variations in ice thickness if a glacier is flowing rapidly. Confirmation of this modelling result over shallow slopes using DInSAR data is shown in Figure 7 Figure 5 c, where measurements characterized by faster ice flow exhibit a steeper dependence of grounding zone width on glacier thickness compared to slower glacier flow. However, due to the sparseness of the DInSAR dataset at steeper slopes, we cannot confirm the modeling derived conclusion for steep sloped bedrock.

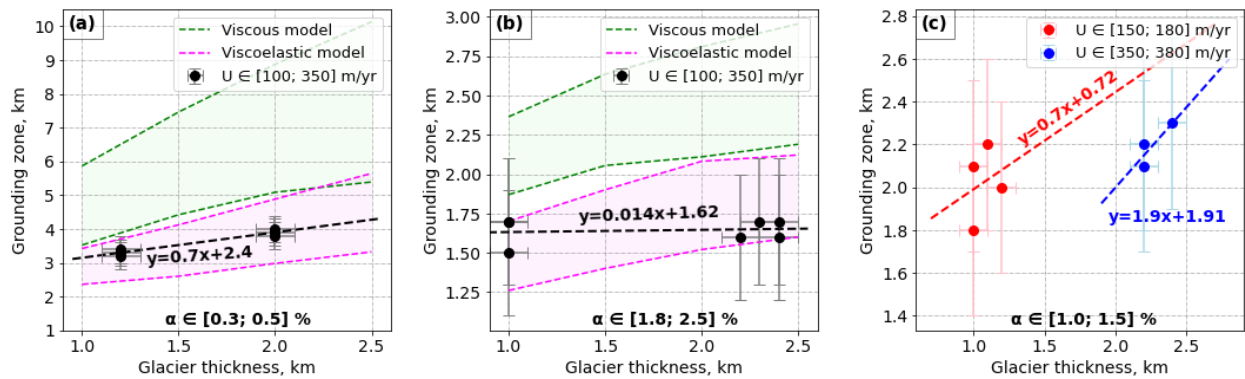


**Figure 7.** Relationship between glacier thickness and DInSAR-derived grounding zone width. (a) DInSAR measurements of grounding zone width (black dots) conducted along profiles characterized by bed slopes ranging from 0.34 to 0.5% and ice flow speeds from 100 to 350 m/year. The black dashed line describes the linear correlation between the ice thickness and DInSAR-derived grounding zones. The green and pink areas represent the grounding zones calculated by the viscous and viscoelastic models, respectively, using the same range of bed slopes and flow speeds as input parameters. (b) The black dots and the dashed line correspond to DInSAR measurements described by bed slopes ranging from 1.86 to 2.5% and ice flow speeds from 100 to 350 m/year, and their linear approximation, respectively. The green and pink areas in (a) and (b) correspond to the grounding zones, calculated by the viscous and viscoelastic models, respectively. (c) DInSAR measurements of grounding zone width (black dots) conducted along profiles characterized by bed slopes ranging from 1.0% to 1.5% and ice flow speeds from 150 to 380 m/year. The black dashed line describes the linear correlation between the ice thickness and DInSAR-derived grounding zones. The green and pink areas represent the grounding zones calculated by the viscous and viscoelastic models, respectively, using the same range of bed slopes and flow speeds as input parameters.

the viscous and viscoelastic models, respectively, for the same range of bed slopes and flow speeds as the DInSAR measurements, where pink and green dashed lines connect the corresponding model outputs. (c) Grounding zone measurements over 1.0 to 1.5% bed slopes, described by [150; 180] m/year and [350; 380] m/year ice flow speeds with corresponding linear approximations.

## **5.2. Role of elasticity**

Using the viscous model for slopes not shallower than 2% can result in overestimating grounding zone widths by up to 25%. For slopes shallower than 2%, the viscous model overestimates grounding zone widths by up to 100% (Figure 6 (c)). The viscous model tends to overestimate the grounding zones compared to the viscoelastic model due to several key factors. The viscoelastic model incorporates both the viscous (fluid-like) and elastic (solid-like) properties of ice, whereas the viscous model neglects the elastic component. This elastic response is fundamental over the tidal time scales, as ice exhibits elastic behavior under short-term deformations, such as those caused by tidal forces (Sayag and Worster, 2011; Warburton et al., 2020). Moreover, for cyclic loading, such as the tidal flexure of ice shelves, repeated loading and unloading make elastic effects significant (MacAyeal et al., 2015; Reeh et al., 2003). Additionally, the viscoelastic model more accurately captures time-dependent behavior by accounting for not only both the immediate elastic response and the delayed viscous response, but also the stress relaxation, a process neglected by purely viscous models (Christmann et al., 2019; MacAyeal et al., 2015). Research studies (Marsh et al., 2014; Reeh et al., 2000, 2003; Wild et al., 2017) confirm our conclusions regarding the critical importance of both viscous and elastic components at tidal timescales as viscoelastic models provide a more accurate representation of tidal bending processes. While viscous models may be adequate for modeling long-term ice sheet evolution, they fail to represent important short-term phenomena such as tidal motion, seasonal cycles, and calving processes, which require the consideration of elastic responses. On the other hand, purely elastic models rely on a crucial simplification: they ignore the internal ice flow within the glacier, treating the glacier as a solid beam. Consequently, purely elastic models cannot realistically represent the complex nature of Antarctic glaciers, where the ice flow velocity in some glaciers exceeds 1 km/year (Rignot et al., 2011). By incorporating the viscous and elastic components in series, known as the Maxwell model of viscoelasticity, both slow and rapid deformations are considered. However, the simple Maxwell model describes small deformations, whereas the deformations of our interest may extend up to 50% of the glacier domain length. Therefore, we applied the upper-convected Maxwell model of viscoelasticity, which includes some geometrical non-linearity and allows the modeling of significantly larger deformations compared to the simple Maxwell model. Building on this, Christmann et al. (2021) emphasize that incorporating both viscous and elastic components is essential for realistic glacier dynamics modeling. In their study, the elastic component is crucial for accurately capturing the physical processes within a glacier, as it accounts for elastic strains in areas with sliding-dominated flow or high vertical deformations (Christmann et al., 2021). A similar argument was made by Hunke and Dukowicz (1997), highlighting that the elastic properties of ice temporarily reduce the overall deformation caused by the viscous component, which explains why the purely viscous model always estimates a wider grounding zone compared to the viscoelastic model. Elastic deformation is a short-term, recoverable response, while viscous deformation is a slower process that dominates over longer timescales. In situations involving short-duration forces, the elastic response can mitigate, but

not eliminate, the visible effects of viscous deformation, providing a temporary reduction in overall glacier strain. This further highlights the necessity of incorporating both components for accurate modeling.

## 6. Conclusion

This study provides a comprehensive analysis of tide-induced grounding line variations across TOT, MU, and REN glaciers in East Antarctica, using both viscous and viscoelastic models. Our results emphasize the crucial role of ice elasticity in modeling grounding zone behavior, particularly for glaciers on shallow bed slopes. Given the 400 m uncertainty on DInSAR-based grounding zone width measurements, the viscoelastic model consistently outperforms the viscous model, capturing 97% of the grounding zone measurements when accounting for the measurement error. Overall, both models can capture the rationally decaying relationship between grounding zone width ( $GZ$ ) and bed slope ( $\alpha$ ), expressed as  $\alpha = a \cdot GZ^b + c$ , where  $a$ ,  $b$ , and  $c$  are fitting parameters. The main difference lies in the dimensionless relaxation parameter  $b$ , which is ~24% smaller for the viscoelastic model, allowing it to better capture the observed dataset behavior. The elastic component introduces a damping effect, temporarily limiting the overall deformation caused by the viscous component (Hunke and Dukowicz, 1997). During a short timescale, the elastic component acts as a buffer, reducing the impact of elastic deformation, especially during cyclic events such as tidal flexure. This effect helps the viscoelastic model to accurately capture short-term glacier deformations and tide-induced grounding zones. On average, the elastic component reduces the tidally induced grounding zone width by half, shielding the grounding zones from the infiltration of warm water that melts the glacier from below (Rignot et al., 2024), thereby promoting a stabilizing effect. Accounting for the DInSAR-derived grounding zone width measurements error, the viscous model may be applied for grounding zone widths of less than 1.5 km and slopes steeper than 3%. For shallower slopes, using a viscous model may lead to a 100% overestimation of the grounding zone width. These findings reinforce the need for incorporating both viscous and elastic components in short-term glacier models to improve the prediction of grounding zone dynamics. Glacier thickness and velocity also influence the grounding zone width, with thicker glaciers and faster flow speeds contributing to wider grounding zones. Increased ice thickness extends the flexural wavelength, enlarging the area affected by tidal forces, while higher glacier velocities amplify elastic stresses, further expanding the grounding zone. These effects are especially pronounced on shallow bed slopes, where even small changes in thickness and velocity can lead to significant variations in grounding zone extent. This research underscores the critical impact of glacier thickness, bed slope, and ice velocity on grounding zone width, with elastic stresses playing a key role in fast-flowing glaciers on shallow slopes. As climate change continues to influence polar regions, this modeling framework offers valuable insights for understanding and predicting grounding zone dynamics and their contributions to global sea level rise. Future research should focus on extending this model to include a broader range of glaciers and further refining the elastic-viscous model, particularly in response to tidal cycles and seasonal variations. This would enhance the model's predictive capability and provide deeper insights into how different environmental factors influence glacier dynamics, improving forecasts of grounding zone behavior and their implications for sea level rise.

Comparing all grounding zone values generated by the viscous and viscoelastic models, we observe a linear relationship between these values, with the grounding zone width obtained from the viscous model being approximately twice that calculated by the viscoelastic model across varying bedrock slopes, glacier thicknesses, and ice inflow speeds. To validate the models' performance, we compare their grounding zone outputs with DInSAR-derived grounding zones over Moscow University, Totten, and Rennick glaciers. To ensure the fair comparison of the models' outputs and the measurements, we input identical bed slope, glacier thickness, and glacier flow speed as those corresponding to these three glaciers and account for respective errors.

Comparison of the grounding zones, obtained from the DInSAR interferograms, with the modeled grounding zones shows that the viscoelastic model achieves significantly higher accuracy than the viscous model. Accounting for the error bars of the DInSAR measurements, the viscoelastic model successfully reproduced  $\sim 93\%$  of all the measurements, while the viscous model succeeds with  $\sim 46\%$  of the measurements. If the error bars are not considered,  $\sim 84\%$  versus  $\sim 13\%$  of the measurements are replicated by the viscoelastic and viscous model, respectively. Therefore, the accuracy of the viscoelastic model outperforms the accuracy of the viscous model by up to  $\sim 71\%$ . Notably, the viscoelastic model reproduces all the measurements over Rennick glacier, either with or without the error bars, while the viscous model fails to replicate a single Rennick grounding zone measurement when the error bars are not included. These observations highlight the significance of incorporating the elastic component in Stokes-based glacier modeling compared to a purely viscous model.

Significant difference between viscous and viscoelastic models can be explained from a continuum mechanics perspective. Viscous response to deformation occurs over long timescales and corresponds to gradual deformations. However, a tidal impact occurs within a single day, rendering tide-induced deformations too rapid for accurate representation by a purely viscous model. Therefore, an element responsible for rapid deformations, or an elastic component, becomes necessary. Putting the viscous and elastic components in series, known as the Maxwell model of viscoelasticity, we ensure that both slow and rapid deformations are taken into account. However, the simple Maxwell model describes small deformations, whereas the deformations of our interest may extend up to 50% of the glacier domain length. Therefore, we applied the upper convected Maxwell model of viscoelasticity, which includes some geometrical non-linearity and allows the modelling of significantly larger deformations compared to the simple Maxwell model.

## Appendix A: Glacier modelling

Here, we provide a detailed description of the viscoelastic model and compare it with the viscous model.

### A1. Principal notation

Notation, used in the paper, is listed in Table A1.

**Table A1.** Models' principal notation

## Code and Data availability

All data needed to evaluate the conclusions in the paper are present in the paper and/or the Supplementary Materials.

We thank the Italian Space Agency (ASI) for providing CSK data (original COSMO-SkyMed product ASI, Agenzia

Spaziale Italiana (2008–2023)). Velocity (<https://nsidc.org/data/NSIDC-0484/versions/2>) and BedMachine (<https://nsidc.org/data/NSIDC-0756/versions/2>) data products are available ~~as MEaSUREs products~~ at the National Snow and Ice Data Center, Boulder CO (NSIDC) [website](#). The source codes for the viscous and viscoelastic models are freely available on <https://github.com/agstub/grounding-line-methods/tree/v1.0.0> and <https://github.com/agstub/viscoelastic-glines> GitHub repositories, respectively. Geocoded interferograms and grounding-line positions are available at <https://doi.org/10.5281/zenodo.10853336>.

## Author contribution

PM and ~~NRM~~ designed the study; AS developed the viscous and viscoelastic models; ~~NRM~~ performed the codes modifications and grounding zone simulations under the supervision of KN and RB; ~~NRM~~ and PM performed the measurement of the grounding zones from the DInSAR data and the assessment of the main ice-bed system parameters; LD provided the CSK DInSAR data; ~~NRM~~ and PM wrote the manuscript draft with contributions from KN, RB and AS reviewed and edited the manuscript. [PM secured research funding.](#)

## Competing interests

The authors declare that they have no conflict of interest.

## Acknowledgements

The research was conducted at the University of Houston, Houston, TX, US [under a contract with the NASA's Cryosphere Program \(NNH23ZDA001N-CRYO\) and the Decadal Survey Incubation Program: Science and Technology \(NNH21ZDA001N-DSI\)](#). We acknowledge the Research Computing Data Core (RCDC) for giving access to advance high-performance computing resources of the University of Houston. We [extend our gratitude to](#) ~~thank~~ the Italian Space Agency (ASI) for providing CSK data (original COSMO-SkyMed product ASI, Agenzia Spaziale Italiana (2008–2023)). [We thank Konnor G. Ross for providing linguistic assistance during the peer-review process. We also thank the two anonymous reviewers for their valuable feedback, which greatly contributed to improving the quality of the manuscript.](#)

## References

- Van Achter, G., Fichefet, T., Goosse, H., Pelletier, C., Sterlin, J., Huot, P.-V., Lemieux, J.-F., Fraser, A. D., Haubner, K., and Porter-Smith, R.: Modelling landfast sea ice and its influence on ocean–ice interactions in the area of the Totten Glacier, East Antarctica, Ocean Model (Oxf), 169, 101920, <https://doi.org/10.1016/j.ocemod.2021.101920>, 2022.
- Aitken, A. R. A., Roberts, J. L., Ommen, T. D. van, Young, D. A., Golledge, N. R., Greenbaum, J. S., Blankenship, D. D., and Siegert, M. J.: Repeated large-scale retreat and advance of Totten Glacier indicated by inland bed erosion, Nature, 533, 385–389, <https://doi.org/10.1038/nature17447>, 2016.



Albrecht, N., Vennell, R., Williams, M., Stevens, C., Langhorne, P., Leonard, G., and Haskell, T.: Observation of sub-inertial internal tides in McMurdo Sound, Antarctica, *Geophys Res Lett*, 33, <https://doi.org/10.1029/2006GL027377>, 2006.

Allen, B., Mayewski, P. A., Lyons, W. B., and Spencer, M. J.: Glaciochemical Studies and Estimated Net Mass Balances for Rennick Glacier Area, Antarctica, *Ann Glaciol*, 7, 1–6, <https://doi.org/10.3189/S0260305500005826>, 1985.

Alnæs, M., Blechta, J., Hake, J., Johansson, A., Kehlet, B., Logg, A., Richardson, C., Ring, J., Rognes, M. E., and Wells, G. N.: The FEniCS project version 1.5, *Archive of numerical software*, 3, 2015.

Bensi, M., Kovačević, V., Donda, F., O’Brien, P. E., Armbrecht, L., and Armand, L. K.: Water masses distribution offshore the Sabrina Coast (East Antarctica), *Earth Syst Sci Data*, 14, 65–78, <https://doi.org/10.5194/essd-14-65-2022>, 2022.

Brancato, V., Rignot, E., Milillo, P., Morlighem, M., Mouginot, J., An, L., Scheuchl, B., Jeong, S., Rizzoli, P., Bueso Bello, J. L., and Prats-Iraola, P.: Grounding Line Retreat of Denman Glacier, East Antarctica, Measured With COSMO-SkyMed Radar Interferometry Data, *Geophys Res Lett*, 47, e2019GL086291, <https://doi.org/10.1029/2019GL086291>, 2020.

Brunt, K. M., Fricker, H. A., Padman, L., Scambos, T. A., and O’Neel, S.: Mapping the grounding zone of the Ross Ice Shelf, Antarctica, using ICESat laser altimetry, *Ann Glaciol*, 51, 71–79, <https://doi.org/10.3189/172756410791392790>, 2010.

Chen, H., Rignot, E., Scheuchl, B., and Ehrenfeucht, S.: Grounding Zone of Amery Ice Shelf, Antarctica, From Differential Synthetic-Aperture Radar Interferometry, *Geophys Res Lett*, 50, e2022GL102430, <https://doi.org/10.1029/2022GL102430>, 2023.

Christmann, J., Muller, R., and Humbert, A.: On nonlinear strain theory for a viscoelastic material model and its implications for calving of ice shelves, *Journal of Glaciology*, 65, 212–224, <https://doi.org/10.1017/jog.2018.107>, 2019.

Christmann, J., Helm, V., Khan, S. A., Kleiner, T., Müller, R., Morlighem, M., Neckel, N., Rückamp, M., Steinhage, D., Zeising, O., and Humbert, A.: Elastic deformation plays a non-negligible role in Greenland’s outlet glacier flow, *Commun Earth Environ*, 2, 232, <https://doi.org/10.1038/s43247-021-00296-3>, 2021.

Coleman, R., Erofeeva, L., Fricker, H. A., Howard, S., and Padman, L.: A new tide model for the Antarctic ice shelves and seas, *Ann Glaciol*, 34, 247–254, <https://doi.org/DOI: 10.3189/172756402781817752>, 2002.

Cornford, S. L., Seroussi, H., Asay-Davis, X. S., Gudmundsson, G. H., Arthern, R., Borstad, C., Christmann, J., Dias dos Santos, T., Feldmann, J., Goldberg, D., Hoffman, M. J., Humbert, A., Kleiner, T., Leguy, G., Lipscomb, W. H., Merino, N., Durand, G., Morlighem, M., Pollard, D., Rückamp, M., Williams, C. R., and Yu, H.: Results of the third Marine Ice Sheet Model Intercomparison Project (MISMIP+), *Cryosphere*, 14, 2283–2301, <https://doi.org/10.5194/tc-14-2283-2020>, 2020.

Davison, B. J., Hogg, A. E., Rigby, R., Veldhuijsen, S., van Wessem, J. M., van den Broeke, M. R., Holland, P. R., Selley, H. L., and Dutrieux, P.: Sea level rise from West Antarctic mass loss significantly modified by large snowfall anomalies, *Nat Commun*, 14, 1479, <https://doi.org/10.1038/s41467-023-36990-3>, 2023.

887 Dawson, G. J. and Bamber, J. L.: Antarctic Grounding Line Mapping From CryoSat-2 Radar Altimetry, *Geophys Res*  
888 *Lett*, 44, 11,886–11,893, <https://doi.org/10.1002/2017GL075589>, 2017.

889 Durand, G., Gagliardini, O., de Fleurian, B., Zwinger, T., and Le Meur, E.: Marine ice sheet dynamics: Hysteresis and  
890 neutral equilibrium, *J Geophys Res*, 114, F03009, <https://doi.org/10.1029/2008JF001170>, 2009.

891 Fernandez, R., Gulick, S., Domack, E., Montelli, A., Leventer, A., Shevenell, A., and Frederick, B.: Past ice stream  
892 and ice sheet changes on the continental shelf off the Sabrina Coast, East Antarctica, *Geomorphology*, 317, 10–22,  
893 <https://doi.org/10.1016/j.geomorph.2018.05.020>, 2018.

894 Freer, B. I. D., Marsh, O. J., Hogg, A. E., Fricker, H. A., and Padman, L.: Modes of Antarctic tidal grounding line  
895 migration revealed by Ice, Cloud, and land Elevation Satellite-2 (ICESat-2) laser altimetry, *Cryosphere*, 17, 4079–  
896 4101, <https://doi.org/10.5194/tc-17-4079-2023>, 2023.

897 Friedl, P., Weiser, F., Fluhner, A., and Braun, M. H.: Remote sensing of glacier and ice sheet grounding lines: A  
898 review, *Earth Sci Rev*, 201, 102948, <https://doi.org/10.1016/j.earscirev.2019.102948>, 2020.

899 Gagliardini, O., Brondex, J., Gillet-Chaulet, F., Tavard, L., Peyaud, V., and Durand, G.: Brief communication: Impact  
900 of mesh resolution for MISMIP and MISMIP3d experiments using Elmer/Ice, *Cryosphere*, 10, 307–312,  
901 <https://doi.org/10.5194/tc-10-307-2016>, 2016.

902 Goldstein, R. M., Engelhardt, H., Kamb, B., and Frolich, R. M.: Satellite Radar Interferometry for Monitoring Ice  
903 Sheet Motion: Application to an Antarctic Ice Stream, *Science* (1979), 262, 1525–1530,  
904 <https://doi.org/10.1126/science.262.5139.1525>, 1993.

905 Gudmundsson, G. H.: Ice-stream response to ocean tides and the form of the basal sliding law, *Cryosphere*, 5, 259–  
906 270, <https://doi.org/10.5194/tc-5-259-2011>, 2011.

907 Haseloff, M. and Sergienko, O. V.: The effect of buttressing on grounding line dynamics, *Journal of Glaciology*, 64,  
908 417–431, <https://doi.org/10.1017/jog.2018.30>, 2018.

909 Hersbach, H., Bell, B., Berrisford, P., Hirahara, S., Horányi, A., Muñoz-Sabater, J., Nicolas, J., Peubey, C., Radu, R.,  
910 Schepers, D., Simmons, A., Soci, C., Abdalla, S., Abellan, X., Balsamo, G., Bechtold, P., Biavati, G., Bidlot, J.,  
911 Bonavita, M., De Chiara, G., Dahlgren, P., Dee, D., Diamantakis, M., Dragani, R., Flemming, J., Forbes, R., Fuentes,  
912 M., Geer, A., Haimberger, L., Healy, S., Hogan, R. J., Hólm, E., Janisková, M., Keeley, S., Laloyaux, P., Lopez, P.,  
913 Lupu, C., Radnoti, G., de Rosnay, P., Rozum, I., Vamborg, F., Villaume, S., and Thépaut, J.: The ERA5 global  
914 reanalysis, *Quarterly Journal of the Royal Meteorological Society*, 146, 1999–2049, <https://doi.org/10.1002/qj.3803>,  
915 2020.

916 Hibbins, R. E., Marsh, O. J., McDonald, A. J., and Jarvis, M. J.: A new perspective on the longitudinal variability of  
917 the semidiurnal tide, *Geophys Res Lett*, 37, <https://doi.org/10.1029/2010GL044015>, 2010.

918 Hirt, C. W. and Nichols, B. D.: Volume of fluid (VOF) method for the dynamics of free boundaries, *J Comput Phys*,  
919 39, 201–225, [https://doi.org/10.1016/0021-9991\(81\)90145-5](https://doi.org/10.1016/0021-9991(81)90145-5), 1981.

920 Holland, P. R.: A model of tidally dominated ocean processes near ice shelf grounding lines, *J Geophys Res Oceans*,  
921 113, <https://doi.org/10.1029/2007JC004576>, 2008.

922 Hunke, E. C. and Dukowicz, J. K.: An Elastic–Viscous–Plastic Model for Sea Ice Dynamics, *J Phys Oceanogr*, 27,  
923 1849–1867, [https://doi.org/10.1175/1520-0485\(1997\)027<1849:AEVPMF>2.0.CO;2](https://doi.org/10.1175/1520-0485(1997)027<1849:AEVPMF>2.0.CO;2), 1997.

Li, T., Dawson, G. J., Chuter, S. J., and Bamber, J. L.: Grounding line retreat and tide-modulated ocean channels at Moscow University and Totten Glacier ice shelves, East Antarctica, *Cryosphere*, 17, 1003–1022, <https://doi.org/10.5194/tc-17-1003-2023>, 2023.

Logg, A., Mardal, K.-A., and Wells, G.: Automated solution of differential equations by the finite element method: The FEniCS book, Springer Science & Business Media, 2012.

Lowry, D. P., Han, H. K., Golledge, N. R., Gomez, N., Johnson, K. M., and McKay, R. M.: Ocean cavity regime shift reversed West Antarctic grounding line retreat in the late Holocene, *Nat Commun*, 15, 3176, <https://doi.org/10.1038/s41467-024-47369-3>, 2024.

MacAyeal, D. R., Sergienko, O. V., and Banwell, A. F.: A model of viscoelastic ice-shelf flexure, *Journal of Glaciology*, 61, 635–645, <https://doi.org/DOI: 10.3189/2015JoG14J169>, 2015.

Marsh, O. J., Rack, W., Golledge, N. R., Lawson, W., and Floricioiu, D.: Grounding-zone ice thickness from InSAR: Inverse modelling of tidal elastic bending, *Journal of Glaciology*, 60, 526–536, <https://doi.org/DOI: 10.3189/2014JoG13J033>, 2014.

Mayewski, P. A., Attig, J. W., and Drewry, D. J.: Pattern of Ice Surface Lowering for Rennick Glacier, Northern Victoria Land, Antarctica, *Journal of Glaciology*, 22, 53–65, <https://doi.org/10.3189/S0022143000014052>, 1979.

Meneghel, M., Bondesan, A., Salvatore, M. C., and Orombelli, G.: A model of the glacial retreat of upper Rennick Glacier, Victoria Land, Antarctica, *Ann Glaciol*, 29, 225–230, <https://doi.org/10.3189/172756499781821463>, 1999.

Miles, B. W. J., Stokes, C. R., Jamieson, S. S. R., Jordan, J. R., Gudmundsson, G. H., and Jenkins, A.: High spatial and temporal variability in Antarctic ice discharge linked to ice shelf buttressing and bed geometry, *Sci Rep*, 12, 10968, <https://doi.org/10.1038/s41598-022-13517-2>, 2022.

Milillo, P., Fielding, E. J., Shulz, W. H., Delbridge, B., and Burgmann, R.: COSMO-SkyMed Spotlight Interferometry Over Rural Areas: The Slumgullion Landslide in Colorado, USA, *IEEE J Sel Top Appl Earth Obs Remote Sens*, 7, 2919–2926, <https://doi.org/10.1109/JSTARS.2014.2345664>, 2014.

Milillo, P., Rignot, E., Mouginot, J., Scheuchl, B., Morlighem, M., Li, X., and Salzer, J. T.: On the Short-term Grounding Zone Dynamics of Pine Island Glacier, West Antarctica, Observed With COSMO-SkyMed Interferometric Data, *Geophys Res Lett*, 44, 10,436–10,444, <https://doi.org/10.1002/2017GL074320>, 2017.

Milillo, P., Rignot, E., Rizzoli, P., Scheuchl, B., Mouginot, J., Bueso-Bello, J., and Prats-Iraola, P.: Heterogeneous retreat and ice melt of Thwaites Glacier, West Antarctica, *Sci Adv*, 5, eaau3433, <https://doi.org/10.1126/sciadv.aau3433>, 2019.

Milillo, P., Rignot, E., Rizzoli, P., Scheuchl, B., Mouginot, J., Bueso-Bello, J. L., Prats-Iraola, P., and Dini, L.: Rapid glacier retreat rates observed in West Antarctica, *Nat Geosci*, 15, 48–53, <https://doi.org/10.1038/s41561-021-00877-z>, 2022.

Minchew, B. M., Simons, M., Riel, B., and Milillo, P.: Tidally induced variations in vertical and horizontal motion on Rutford Ice Stream, West Antarctica, inferred from remotely sensed observations, *J Geophys Res Earth Surf*, 122, 167–190, <https://doi.org/10.1002/2016JF003971>, 2017.

959 Mohajerani, Y., Velicogna, I., and Rignot, E.: Mass Loss of Totten and Moscow University Glaciers, East Antarctica,  
 960 Using Regionally Optimized GRACE Mascons, *Geophys Res Lett*, 45, 7010–7018,  
 961 <https://doi.org/10.1029/2018GL078173>, 2018.

962 Morlighem, M., Williams, C. N., Rignot, E., An, L., Arndt, J. E., Bamber, J. L., Catania, G., Chauché, N., Dowdeswell,  
 963 J. A., Dorschel, B., Fenty, I., Hogan, K., Howat, I., Hubbard, A., Jakobsson, M., Jordan, T. M., Kjeldsen, K. K.,  
 964 Millan, R., Mayer, L., Mouginot, J., Noël, B. P. Y., O’Cofaigh, C., Palmer, S., Rysgaard, S., Seroussi, H., Siegert, M.  
 965 J., Slabon, P., Straneo, F., van den Broeke, M. R., Weinrebe, W., Wood, M., and Zinglensen, K. B.: BedMachine v3:  
 966 Complete Bed Topography and Ocean Bathymetry Mapping of Greenland From Multibeam Echo Sounding Combined  
 967 With Mass Conservation, *Geophys Res Lett*, 44, 11–51, <https://doi.org/10.1002/2017GL074954>, 2017.

968 Orsi, A. H. and Webb, C. J.: Impact of Sea Ice Production off Sabrina Coast, East Antarctica, *Geophys Res Lett*, 49,  
 969 e2021GL095613, <https://doi.org/10.1029/2021GL095613>, 2022.

970 Padman, L., Fricker, H. A., Coleman, R., Howard, S., and Erofeeva, L.: A new tide model for the Antarctic ice shelves  
 971 and seas, *Ann Glaciol*, 34, 247–254, <https://doi.org/10.3189/172756402781817752>, 2002.

972 Padman, L., Siegfried, M. R., and Fricker, H. A.: Ocean Tide Influences on the Antarctic and Greenland Ice Sheets,  
 973 *Reviews of Geophysics*, 56, 142–184, <https://doi.org/10.1002/2016RG000546>, 2018.

974 Pritchard, H. D., Arthern, R. J., Vaughan, D. G., and Edwards, L. A.: Extensive dynamic thinning on the margins of  
 975 the Greenland and Antarctic ice sheets, *Nature*, 461, 971–975, <https://doi.org/https://doi.org/10.1038/nature08471>,  
 976 2009.

977 Pritchard, H. D., Ligtenberg, S. R. M., Fricker, H. A., Vaughan, D. G., van den Broeke, M. R., and Padman, L.:  
 978 Antarctic ice-sheet loss driven by basal melting of ice shelves, *Nature*, 484, 502–505,  
 979 <https://doi.org/10.1038/nature10968>, 2012.

980 Reeh, N., Mayer, C., Olesen, O. B., Christensen, E. L., and Thomsen, H. H.: Tidal movement of Nioghalvfjerdsfjorden  
 981 glacier, northeast Greenland: observations and modelling, *Ann Glaciol*, 31, 111–117, [https://doi.org/DOI:](https://doi.org/DOI:10.3189/172756400781820408)  
 982 [10.3189/172756400781820408](https://doi.org/DOI:10.3189/172756400781820408), 2000.

983 Reeh, N., Christensen, E. L., Mayer, C., and Olesen, O. B.: Tidal bending of glaciers: a linear viscoelastic approach,  
 984 *Ann Glaciol*, 37, 83–89, [https://doi.org/DOI: 10.3189/172756403781815663](https://doi.org/DOI:10.3189/172756403781815663), 2003.

985 Rignot, E. and Thomas, R. H.: Mass Balance of Polar Ice Sheets, *Science* (1979), 297, 1502–1506,  
 986 <https://doi.org/10.1126/science.1073888>, 2002.

987 Rignot, E., Mouginot, J., and Scheuchl, B.: Ice flow of the Antarctic ice sheet, *Science* (1979), 333, 1427–1430, 2011.

988 Rignot, E., Jacobs, S., Mouginot, J., and Scheuchl, B.: Ice-Shelf Melting Around Antarctica, *Science* (1979), 341,  
 989 266–270, <https://doi.org/10.1126/science.1235798>, 2013.

990 Rignot, E., Mouginot, J., Morlighem, M., Seroussi, H., and Scheuchl, B.: Widespread, rapid grounding line retreat of  
 991 Pine Island, Thwaites, Smith, and Kohler glaciers, West Antarctica, from 1992 to 2011, *Geophys Res Lett*, 41, 3502–  
 992 3509, <https://doi.org/10.1002/2014GL060140>, 2014.

993 Rignot, E., Mouginot, J., and Scheuchl, B.: MEaSUREs Antarctic Grounding Line from Differential Satellite Radar  
 994 Interferometry, Version 2, Nat. Snow and Ice Data Center, <https://doi.org/https://doi.org/10.5067/IKBWW4RYHF1Q>,  
 995 2016.

996 Rignot, E., Mouginot, J., and Scheuchl, B.: MEaSUREs InSAR-based Antarctica ice velocity map, version 2, Nat.  
 997 Snow Ice Data Center, <https://doi.org/https://doi.org/10.5067/D7GK8F5J8M8R>, 2017.

998 Rignot, E., Mouginot, J., Scheuchl, B., van den Broeke, M., van Wessem, M. J., and Morlighem, M.: Four decades of  
 999 Antarctic Ice Sheet mass balance from 1979–2017, *Proceedings of the National Academy of Sciences*, 116, 1095–  
 1000 1103, <https://doi.org/10.1073/pnas.1812883116>, 2019.

1001 Rignot, E., Ciraci, E., Scheuchl, B., Tolpekin, V., Wollersheim, M., and Dow, C.: Widespread seawater intrusions  
 1002 beneath the grounded ice of Thwaites Glacier, West Antarctica, *Proceedings of the National Academy of Sciences*,  
 1003 121, e2404766121, <https://doi.org/10.1073/pnas.2404766121>, 2024.

1004 Roberts, J., Galton-Fenzi, B. K., Paolo, F. S., Donnelly, C., Gwyther, D. E., Padman, L., Young, D., Warner, R.,  
 1005 Greenbaum, J., Fricker, H. A., Payne, A. J., Cornford, S., Le Brocq, A., van Ommen, T., Blankenship, D., and Siegert,  
 1006 M. J.: Ocean forced variability of Totten Glacier mass loss, *Geological Society, London, Special Publications*, 461,  
 1007 175–186, <https://doi.org/10.1144/SP461.6>, 2018.

1008 Rosier, S. H. R. and Gudmundsson, G. H.: Exploring mechanisms responsible for tidal modulation in flow of the  
 1009 Filchner–Ronne Ice Shelf, *Cryosphere*, 14, 17–37, <https://doi.org/10.5194/tc-14-17-2020>, 2020.

1010 Rosier, S. H. R., Gudmundsson, G. H., and Green, J. A. M.: Insights into ice stream dynamics through modelling their  
 1011 response to tidal forcing, *Cryosphere*, 8, 1763–1775, <https://doi.org/10.5194/tc-8-1763-2014>, 2014.

1012 Ross, N., Milillo, P., and Dini, L.: Automated grounding line delineation using deep learning and phase gradient-based  
 1013 approaches on COSMO-SkyMed DInSAR data, *Remote Sens Environ*, 315, 114429,  
 1014 <https://doi.org/https://doi.org/10.1016/j.rse.2024.114429>, 2024.

1015 Sayag, R. and Worster, M. G.: Elastic response of a grounded ice sheet coupled to a floating ice shelf, *Phys Rev E*,  
 1016 84, 036111, <https://doi.org/10.1103/PhysRevE.84.036111>, 2011.

1017 Sayag, R. and Worster, M. G.: Elastic dynamics and tidal migration of grounding lines modify subglacial lubrication  
 1018 and melting, *Geophys Res Lett*, 40, 5877–5881, <https://doi.org/10.1002/2013GL057942>, 2013.

1019 Schoof, C.: Ice sheet grounding line dynamics: Steady states, stability, and hysteresis, *J Geophys Res*, 112, F03S28,  
 1020 <https://doi.org/10.1029/2006JF000664>, 2007.

1021 Schoof, C.: Marine ice sheet dynamics. Part 2. A Stokes flow contact problem, *J Fluid Mech*, 679, 122–155,  
 1022 <https://doi.org/10.1017/jfm.2011.129>, 2011.

1023 Sergienko, O. and Haseloff, M.: ‘Stable’ and ‘unstable’ are not useful descriptions of marine ice sheets in the Earth’s  
 1024 climate system, *Journal of Glaciology*, 69, 1483–1499, <https://doi.org/10.1017/jog.2023.40>, 2023.

1025 Sergienko, O. V.: No general stability conditions for marine ice-sheet grounding lines in the presence of feedbacks,  
 1026 *Nat Commun*, 13, 2265, <https://doi.org/10.1038/s41467-022-29892-3>, 2022.

1027 Seroussi, H., Morlighem, M., Larour, E., Rignot, E., and Khazendar, A.: Hydrostatic grounding line parameterization  
 1028 in ice sheet models, *Cryosphere*, 8, 2075–2087, <https://doi.org/10.5194/tc-8-2075-2014>, 2014.

1029 Snoeijer, J. H., Pandey, A., Herrada, M. A., and Eggers, J.: The relationship between viscoelasticity and elasticity,  
 1030 *Proceedings of the Royal Society A: Mathematical, Physical and Engineering Sciences*, 476, 20200419,  
 1031 <https://doi.org/10.1098/rspa.2020.0419>, 2020.



Stubblefield, A. G., Spiegelman, M., and Creyts, T. T.: Variational formulation of marine ice-sheet and subglacial-lake grounding-line dynamics, *J Fluid Mech*, 919, A23, <https://doi.org/10.1017/jfm.2021.394>, 2021.

Sturm, A. and Carrier, S. J.: Geology of the region between the Matusevich and Tucker Glaciers, north Victoria Land, Antarctica, *New Zealand Journal of Geology and Geophysics*, 13, 408–435, <https://doi.org/10.1080/00288306.1970.10423977>, 1970.

Tsai, V. C. and Gudmundsson, G. H.: An improved model for tidally modulated grounding-line migration, *Journal of Glaciology*, 61, 216–222, <https://doi.org/10.3189/2015JoG14J152>, 2015.

Warburton, K. L. P., Hewitt, D. R., and Neufeld, J. A.: Tidal Grounding-Line Migration Modulated by Subglacial Hydrology, *Geophys Res Lett*, 47, e2020GL089088, <https://doi.org/10.1029/2020GL089088>, 2020.

Werner, C., Wegmüller, U., Strozzi, T., and Wiesmann, A.: Gamma SAR and interferometric processing software, in: *Proceedings of the ers-envisat symposium*, Gothenburg, Sweden, 1620, 2000.

Wild, C. T., Marsh, O. J., and Rack, W.: Viscosity and elasticity: a model intercomparison of ice-shelf bending in an Antarctic grounding zone, *Journal of Glaciology*, 63, 573–580, <https://doi.org/DOI: 10.1017/jog.2017.15>, 2017.